

Spitzer IRS spectra of a large sample of Seyfert galaxies: a variety of infrared SEDs in the local AGN population

Catherine L. Buchanan¹, Jack F. Gallimore², Christopher P. O’Dea¹, Stefi A. Baum³, David J. Axon¹, Andrew Robinson¹, Moshe Elitzur⁴, & Martin Elvis⁵

ABSTRACT

We are conducting a large observing program with the Spitzer Space Telescope to determine the mid-to-far infrared spectral energy distributions of a well-defined sample of 87 nearby, 12 μm -selected Seyfert galaxies. In this paper we present the results of IRS low-resolution spectroscopy of a statistically representative subsample of 51 of the galaxies (59%), with an analysis of the continuum shapes and a comparison of the Seyfert types. We find that the spectra clearly divide into groups based on their continuum shapes and spectral features. The largest group (47% of the sample of 51) shows very red continuum suggestive of cool dust and strong emission features attributed to PAHs. Sixteen objects (31%) have a power-law continuum with spectral indices $\alpha_{5-20\mu\text{m}} = -2.3$ – -0.9 that flatten to $\alpha_{20-35\mu\text{m}} = -1.1$ – 0.0 at $\sim 20\mu\text{m}$. Clear silicate emission features at 10 and 18 μm are found in two of these objects (Mrk 6 and Mrk 335). A further 16% of the sample show power-law continua with unchanging slopes of $\alpha_{5-35\mu\text{m}} = -1.7$ – -1.1 . Two objects are dominated by a broad silicate absorption feature. One object in the sample shows an unusual spectrum dominated by emission features, that is unlike any of the other spectra. Some spectral features are clearly related to a starburst contribution to the IR spectrum, while the mechanisms producing observed power-law continuum shapes, attributed to an AGN component, may be dust or non-thermal emission. The infrared spectral types appear to be related to the Seyfert types. Principal component analysis results suggest that the relative contribution of starburst emission may be the dominant cause of variance in the observed spectra. The derived starburst component of each spectrum, however, contributes $<40\%$ of the total flux density. We compare the IR emission with the optically thin radio emission associated with the AGN and find that Sy 1’s have higher ratios of IR/radio emission than Sy 2’s, as predicted by the

¹Department of Physics, Rochester Institute of Technology, 54 Lomb Memorial Drive, Rochester NY 14623. Email: clbps@cis.rit.edu

²Bucknell University Department of Physics, Moore Avenue, Lewisburg, PA 17837

³Center for Imaging Science, Rochester Institute of Technology, 84 Lomb Memorial Drive, Rochester NY 14623. Email: clbps@cis.rit.edu

⁴University of Kentucky Physics & Astronomy Department, Lexington, KY 40506

⁵Harvard-Smithsonian Center for Astrophysics, 60 Garden St., Cambridge, MA 02138

unified model if the torus is optically thick in the mid-IR. However, smooth-density torus models predict a much larger difference between type 1’s and 2’s than the factor of 2 difference observed in our sample; the observed factor of ~ 2 difference between the type 1’s and 2’s in their IR/radio ratios above $15 \mu\text{m}$ requires the standard smooth-density torus models to be optically thin at these wavelengths. However, the resulting low torus opacity requires that the high observed columns detected in X-ray absorption be produced in gas with very low dust to gas ratio (perhaps within the dust sublimation region). On the other hand, our observations may be consistent with clumpy torus models containing a steep radial distribution of optically thick dense clumps. The selection of our sample at $12 \mu\text{m}$, where the torus may be optically thick, implies that there may be orientation-dependent biases in the sample, however we do not find that the sample is biased towards Sy 2’s with more luminous central engines as would be expected. We find that the Sy 2’s typically show stronger starburst contributions than the Sy 1’s in the sample, contrary to what is expected based on the unified scheme for AGN. This may be due to the selection effect that only those Seyfert 2’s with strong starburst contributions had high enough integrated $12 \mu\text{m}$ flux densities to fall above the flux limit of the sample.

Subject headings: galaxies: Seyfert — galaxies: spiral — infrared: galaxies

1. Introduction

Active galactic nuclei (AGNs) are powered by accretion onto a massive black hole (see reviews by Rees 1984 and Shields 1999). The fuel itself is probably ISM from the host galaxy that is driven to the center by bar-induced torques (Jogee et al. 2005), galaxy interactions, or galaxy mergers (Osterbrock 1993 and references therein). Starbursts may be an inevitable consequence of the gas infall (Rees 1984; Norman & Scoville 1988), and the observed relation between black hole mass and host bulge mass in AGNs suggests that nuclear activity is closely connected to star formation (Merritt & Ferrarese 2001; Gebhardt et al. 2000). Nuclear activity, though probably short-lived compared with the lifetime of the host ($\sim 5 - 20\%$ percent of galaxies host AGN; Maiolino & Rieke 1995; Ho et al. 1997; Kauffmann et al. 2003; Hao et al. 2005a), may be an integral part of the evolution of all galaxies. Understanding the inner workings of AGNs and the AGN/starburst connection is therefore important for understanding galaxy evolution.

Seyfert galaxies are the nearest and brightest AGNs and so are well-suited for studying the connection between nuclear activity and star formation. Obscuring dust however hampers studies of the optical – soft X-ray emission produced by young stars and the accretion disk. Emission at infrared wavelengths does not suffer such large extinction, and, further, the dust that absorbs the shorter wavelength emission reradiates in the IR and correspondingly produces a substantial fraction of the bolometric flux of the object. Dissecting the detailed IR spectral energy distribution

(SED) of Seyfert galaxies can reveal the properties of the dust in the nuclear region as well as place constraints on the optical – soft X-ray spectrum (i.e., starburst and AGN spectrum) that heats the dust.

A key factor in understanding Seyfert galaxies is determining the geometry of the nuclear obscuring material. Unification schemes postulate that the observed differences between Seyfert types 1 and 2, such as optical emission line widths and X-ray spectral slopes, are due to orientation-dependent obscuration (see reviews by Urry & Padovani 1995; Antonucci 1993). Alternatively, there may be fundamental differences between the central engines of Sy 1’s and 2’s. The obscuring medium has been modeled as a dusty torus which, viewed edge-on (Sy 2’s), obscures the nucleus but, viewed face-on (Sy 1’s), allows the nucleus to be seen. The inner scale of the torus is thought to be of order 1 pc (e.g., Krolik & Begelman 1988; Gallimore et al. 1999; Ulvestad et al. 1999; Jaffe et al. 2004; Röttgering et al. 2005), but other properties are poorly constrained owing to angular resolution limitations. However, the geometry and equatorial opacity of the torus should have an observable impact on the shape of the infrared SED (Pier & Krolik 1992; Granato & Danese 1994; Ivezić & Elitzur 1997; Nenkova et al. 2002). Thus AGN unification can be tested by comparing the SEDs of type 1 and 2 Seyferts with model predictions.

A third possibility is that the Seyfert types are connected by evolution: an active nucleus evolves through a starburst (type 2) phase during which it is heavily obscured, and into an AGN phase (type 1) when the obscuring dust has been evacuated from the nucleus by starburst-driven winds and AGN outflows (Sanders et al. 1988; Storchi-Bergmann et al. 2001). Supporting this picture is evidence that Seyfert 2’s have significantly more star formation than Seyfert 1’s. Photometric studies have found that Sy 2’s have fainter nuclear infrared emission than Sy 1’s and SEDs consistent with starburst-dominated IR emission, while Sy 1’s have SEDs consistent with pure AGN + quiescent galaxy emission (Edelson, Malkan, & Rieke 1987; Maiolino et al. 1995). However, as orientation is also likely to play a role in the differences between Seyfert 1s and 2s, it is important to investigate the relative contributions of star formation and the active nucleus to the infrared emission in order to test both AGN unification and evolutionary schemes.

The Spitzer space telescope represents a significant step forward in both sensitivity and spatial resolution compared with previous thermal infrared missions. We are conducting a large observing program with the Spitzer space telescope to determine the mid-to-far infrared (MFIR) spectral energy distributions (SEDs) of 87 Seyfert galaxies (PI: J. Gallimore, PID: 3269). The majority of the IRS spectra have been observed (51 objects, 59%), allowing the first statistical analysis of the detailed mid-infrared (MIR) SEDs of a relatively unbiased sample of Seyfert galaxies. In this paper we present an overview of the continuum properties of the sample, and relate these to the optical spectral types. An atlas of spectra and detailed modeling of individual spectra will be presented in a future paper when all data are available. The purpose of this paper is to present the results of our initial analysis of the spectra in order for them to be useful to the AGN community. In §2 we briefly describe the sample properties. The observations and the data reduction are presented in §3. §4 presents typical spectra and an analysis of the continuum shapes. In §5 we discuss the implications

of our results for the unification of Seyfert galaxies and our understanding of the nature of the torus.

2. The Seyfert sample and its properties

The sample of Seyfert galaxies used for this study comprises all Seyfert galaxies from the extended 12 μm sample of Rush et al. (1993) that have $cz < 10000 \text{ km s}^{-1}$. The potential advantage of the 12 μm sample is its perceived resistance to wavelength-dependent selection effects (Spinoglio & Malkan 1989). The redshift criterion was included to ensure that the smallest possible physical size was probed by the fixed Spitzer apertures in order to better exclude host galaxy emission. The resulting sample contains 87 sources. Three of the sample galaxies, NGC 1097, NGC 1566, and NGC 5033, are being extensively observed as part of the SINGS Legacy project, so we are obtaining data for 84 galaxies. The data include IRAC imaging, IRS spectral mapping, and MIPS SED spectra. The present paper discusses the 51 objects in the sample for which 5 – 35 μm IRS spectra are currently available.

The spectral classifications were obtained from the Véron-Cetty & Véron (2003) catalog, and thus have not been made using homogeneous datasets of consistent quality. In several cases, the classification is ambiguous, and we have adopted revised classifications from other sources (Tran 2003; Ho et al. 1997; Veilleux et al. 1995; Phillips 1979). Seven objects in the sample have been reclassified as non-Seyferts (LINERs or star-forming galaxies): MCG +0 – 29 – 23, NGC 4922, NGC 5953, NGC 7130, NGC 7496, NGC 7590, and UGC 11680. These objects have been excluded from analyses comparing Sy 1’s and Sy 2’s, and we expect the results will not be sensitive to the classifications of these objects. For the purposes of comparing the Seyfert types we consider Seyfert types 1.*n* (i.e. types 1.0, 1.2, 1.5, 1.8, and 1.9 as well as narrow line Seyfert 1’s) to be Sy 1’s, and objects with no broad permitted lines or with hidden broad line regions (HBLRs) to be Sy 2’s.

Figures 1 and 2 show the distributions of the IRAS 12 μm flux densities and redshifts of the sample objects. Data for the whole sample are shown, with the objects observed to date with Spitzer ($\sim 50\%$ of the sample) indicated by hatching for comparison. Sy 1’s and Sy 2’s are shown separately. Two-sample statistical tests were performed to determine whether the distributions of flux density and redshift are similar for the Seyfert types and if the objects observed to date are representative of the 12 μm sample as a whole. The probabilities of the various datasets being drawn from the same parent population were calculated using the ASURV package (Lavalley et al. 1992), which enables the analysis of data in which limits are present (Feigelson & Nelson 1985). The results of Gehan and logrank tests are shown in Table 1. We find no significant differences between Sy 1’s and Sy 2’s in either the IRAS 12 μm flux density or redshift distributions. We also find no significant differences between the observed subsample and the whole sample, indicating that the current dataset is broadly representative of the complete sample.

The optically thin nuclear radio emission may be considered an isotropic property of Seyfert

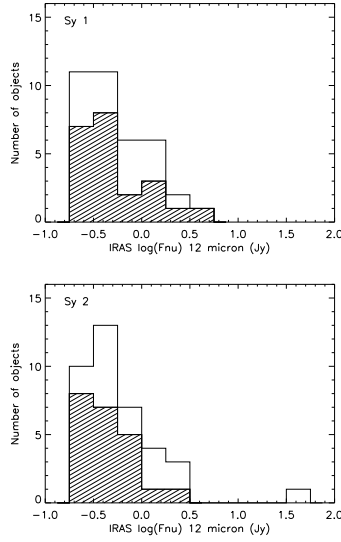


Fig. 1.— Distribution of the IRAS 12 μm fluxes for the Seyfert 1's (*top*) and the Seyfert 2's (*bottom*). Hashed regions indicate the objects with IRS data in hand. Two-sample statistical tests show no significant difference between the Sy 1's and Sy 2's or between the observed objects and the whole sample (Table 1).

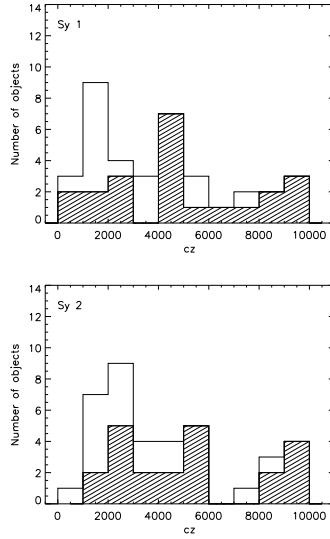


Fig. 2.— Distribution of redshifts for the 12 micron sample. Seyfert 1's (*top*) and Seyfert 2's (*bottom*) are shown separately. Hashed regions indicate the objects with IRS data in hand. Two-sample statistical tests show no significant difference between the Sy 1's and Sy 2's or between the observed objects and the whole sample (Table 1).

galaxies, that provides an orientation-independent measurement of the energy output of the active nucleus (Xu et al. 1999; Edelson 1987; Giuricin et al. 1990; Kukula et al. 1995; Thean et al. 2001). Radio observations of the 12 μm Seyfert sample have been obtained by Thean et al. (2000), using the VLA A array at 8.4 GHz. These high spatial resolution ($0.25''$), high frequency observations isolate the nuclear radio emission ($< 3.5''$ in extent) associated with the AGN from radio emission associated with star formation in the host galaxy. Seyfert nuclei are relatively weak radio emitters, so the larger scale radio emission associated with star formation can dominate over the nuclear radio emission at lower spatial resolutions. Figure 3 shows the distributions of nuclear radio flux densities for the whole sample and for the objects for which we have IRS data in hand. Sy 1’s and Sy 2’s are shown separately. Limits are shown for 4 objects not detected by Thean et al. (2000). Radio flux densities for 6 objects not observed by Thean et al. (2000) were obtained from NED. These were generally lower resolution and lower frequency, and so upper limits to the flux density at 8.4 GHz were derived assuming $S_\nu \propto \nu^{-0.7}$. We find no significant difference between the distributions of nuclear radio flux density for the type 1 and 2 Seyferts. Results of statistical comparisons of sample properties are summarized in Table 1.

3. Observations and Spectral Extraction

The sample galaxies were observed by Spitzer IRS (Houck et al. 2004) in mapping mode, using the Short-Low and Long-Low modules. The modules cover a wavelength range of $\sim 5 - 35 \mu\text{m}$, with a resolving power of 64 – 128. The raw data were processed by the Spitzer pipeline version 11.0. The nuclear spectra were extracted from the Basic Calibrated Data (BCDs) using SMART (Higdon et al. 2004). Preliminary spectral maps show that the surface brightness is dominated by a central point source at these wavelengths, so the default point source aperture was used for the extractions. Only three of the sources (NGC 1365, NGC 5005, & NGC 5953) show a noticeable drop in flux between the overlapping LL (long-low) and SL (short-low) module spectra, which results from extended flux contributing to the wider LL module slit (SL: $3.5''$, LL: $10.5''$). This supports our conclusion that the objects are dominated by the central point source, and so default point source extractions are appropriate. Flux densities were calibrated based on flux calibration tables provided by the Spitzer Science Center. The spectra are shown in Figure 4, grouped according to their shape (see §4.2). The full spectral maps will be presented in a future paper.

Following a suggestion from the referee, comparison of the flux densities of the nuclear IRS spectra with IRAC 5.8 and $8.0 \mu\text{m}$ nuclear photometry (Gallimore et al. 2005, in preparation) later revealed that the spectra underestimated the source flux densities. We attribute this to slit losses that vary as a function of wavelength due to the increasing size of the point spread function with increasing wavelength. As these spectra were obtained in mapping mode, no attempt was made to center the nuclear point source in the slit during the observations. Thus the nuclear (central) slit position is not necessarily well centered on the source and the spectra suffer wavelength-dependent slit losses, up to 20%. This is only a problem for strongly point-source dominated sources. We have

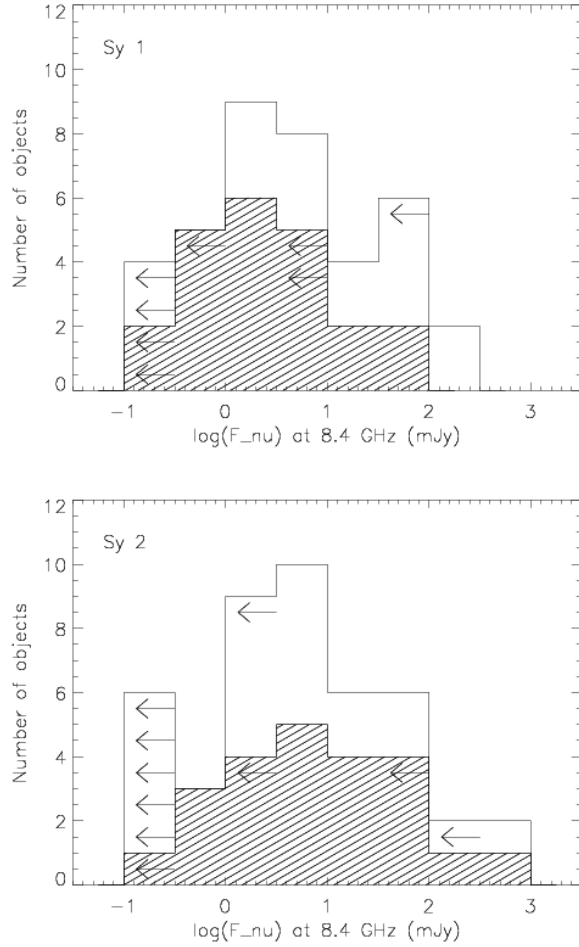


Fig. 3.— Distribution of nuclear radio flux densities for the 12 micron sample. Seyfert 1's (*top*) and Seyfert 2's (*bottom*) are shown separately. Hashed regions indicate the objects with IRS data in hand and arrows indicate upper limits. The results of two-sample tests comparing distributions are shown in Table 1.

attempted to account for this by producing a spectral image cube from the Basic Calibrated Data FITS files of all the slit positions (after background subtraction using the off orders) and iteratively determining an interpolated nuclear image based on the fractional shift perpendicular to the slit that produced the most total flux in the interpolated image. A simplex maximization technique was used to find the optimum interpolated position, which defined the plane containing the spectral image of the point source. We refer to the spectra extracted from the spectral image of the point source as “pointing-corrected” nuclear spectra. Flux densities derived from the resulting pointing-corrected spectra agree well with our IRAC photometry, within 20% for the vast majority of objects and 30-45% for a few objects. The IRS-derived flux densities both overestimate and underestimate the IRAC 5.8 and 8.0 μm point source flux densities, indicating that the flux calibration of our IRS spectra is not systematically underestimating the true flux densities. Excluding the comparison with IRAS (§4.1), in the remainder of the paper the analysis was performed on the original (not pointing-corrected) spectra. Despite the fact that the flux errors are wavelength-dependent, we find that the overall shapes of the spectra are not changed significantly by the pointing correction. We do not expect that the flux errors will have a significant impact on the results.

Table 1. Properties of the sample: results of two-sample tests.

Variable	Group 1	Group 2		Group 1			Group 2		p	p	Figure
[1]	[2]	[3]	n_{lim}	Mean	Median	n_{lim}	Mean	Median	(Gehan)	(Logrank)	[12]
			[4]	[5]	[6]	[7]	[8]	[9]	[10]	[11]	
IRAS $\log(F_{12} \mu\text{m})$ (Jy)	all Sy 1's	all Sy 2's	0	-0.28	-0.37	0	-0.23	-0.35	0.63	0.60	1
IRAS $\log(F_{12} \mu\text{m})$ (Jy)	obs Sy 1's	obs Sy 2's	0	-0.31	-0.39	0	-0.34	-0.42	0.99	0.62	1
IRAS $\log(F_{12} \mu\text{m})$ (Jy)	all Sy 1's	obs Sy 1's	0	-0.28	-0.37	0	-0.31	-0.39	0.69	0.90	1
IRAS $\log(F_{12} \mu\text{m})$ (Jy)	all Sy 2's	obs Sy 2's	0	-0.23	-0.35	0	-0.34	-0.42	0.30	0.26	1
z	all Sy 1's	all Sy 2's	0	0.0139	0.0133	0	0.0143	0.0117	0.80	0.99	2
z	obs Sy 1's	obs Sy 2's	0	0.0169	0.0162	0	0.0171	0.0172	0.83	0.99	2
z	all Sy 1's	obs Sy 1's	0	0.0139	0.0133	0	0.0169	0.0162	0.23	0.29	2
z	all Sy 2's	obs Sy 2's	0	0.0143	0.0117	0	0.0171	0.0172	0.22	0.28	2
$\log(S_{8.4 \text{ GHz}})$ (mJy)	all Sy 1's	all Sy 2's	8	0.57*	0.51	6	0.83*	0.88	0.20	0.29	3
$\log(S_{8.4 \text{ GHz}})$ (mJy)	obs Sy 1's	obs Sy 2's	5	0.40*	0.40	2	0.89*	1.05	0.05	0.11	3
$\log(S_{8.4 \text{ GHz}})$ (mJy)	all Sy 1's	obs Sy 1's	8	0.57*	0.51	5	0.40*	0.40	0.46	0.48	3
$\log(S_{8.4 \text{ GHz}})$ (mJy)	all Sy 2's	obs Sy 2's	6	0.83*	0.88	2	0.89*	1.05	0.73	0.73	3

Note. — Generalized Wilcoxon and Logrank two-sample tests were used to determine the probability that the values of the variable (column [1]) in groups 1 and 2 (columns [2] and [3]) were drawn from the same parent distribution. The number of objects in the groups are: all Sy 1's: 37; observed Sy 1's: 22; all Sy 2's: 38; observed Sy 2's: 22. Columns [4]-[6] list the parameters for group 1: the number of limits in the data, the mean value and the median value, derived using the Kaplan-Meier (K-M) estimator. * Indicates the mean is biased because the lower- or uppermost limit was changed to a detection to compute the K-M distribution. Columns [7]-[9] list the same parameters for group 2. Large values of p (columns [10] and [11]) indicate there is no significant difference between the distributions for the two groups. Column [12] refers to the Figure number showing the distribution in the variables.

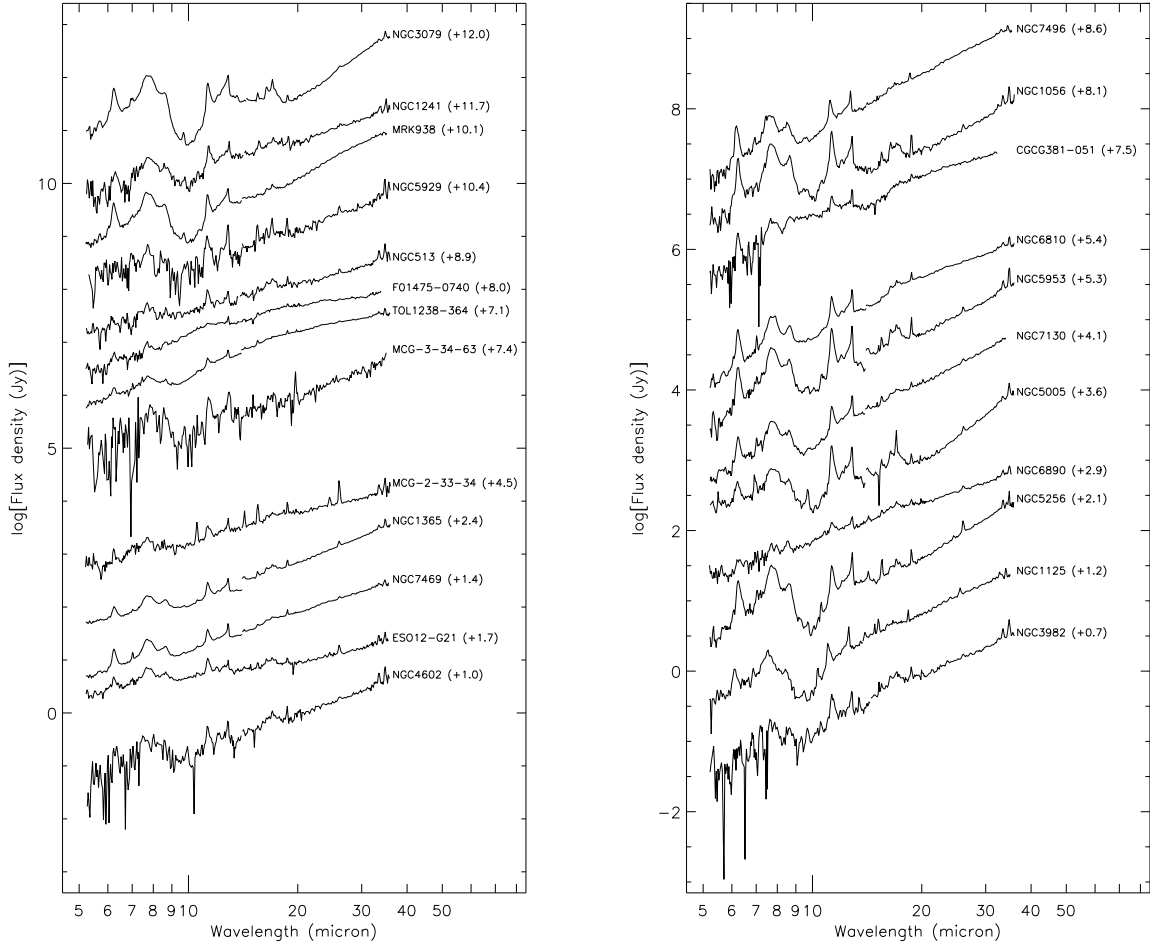


Fig. 4.— (a) Spectra dominated by red continuum and PAH features. Each spectrum is labeled with the object name and the flux density offset applied.

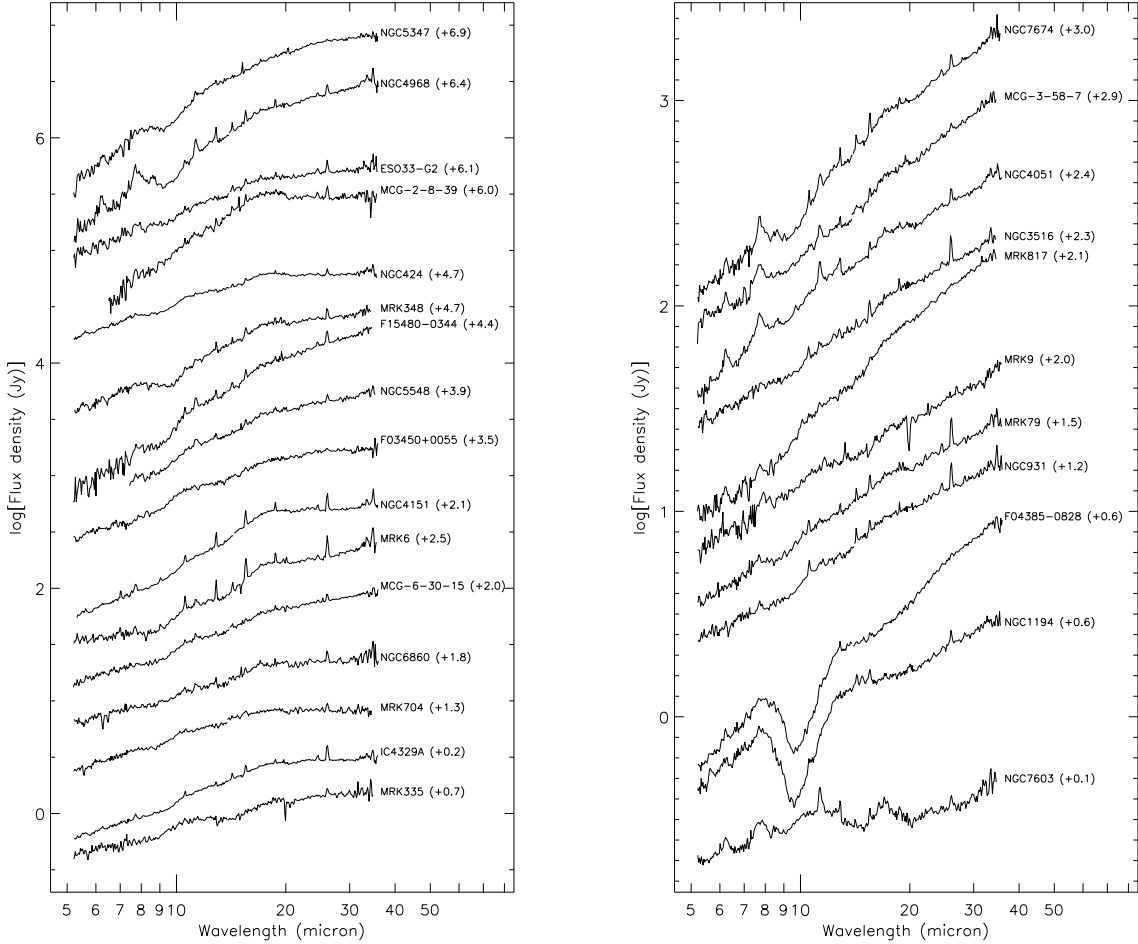


Fig. 4.— (a) The left panel shows spectra that may be described by a broken power law continuum. The right panel shows spectra that can be fitted with a continuous power law, the two spectra showing silicate absorption at $10 \mu\text{m}$, and the ungrouped spectrum (bottom). Each spectrum is labeled with the object name and the flux density offset applied.

4. Results

4.1. Comparison with IRAS

The IRS apertures are much smaller than those of IRAS, and so we can evaluate the fraction of extended flux not included in the IRS aperture (assuming insignificant mid-infrared variation in the ~ 24 years between observations). The IRS spectra span the wavelength range $5 - 35 \mu\text{m}$, so 12 and $25 \mu\text{m}$ nuclear flux densities corresponding to the IRAS bandpasses can be derived from the nuclear spectra. For the purposes of this comparison, the nuclear flux densities were determined using the pointing-corrected IRS spectra and the IRAS bandpass spectral response functions. The distributions of nuclear 12 and $25 \mu\text{m}$ flux densities for Sy 1’s and Sy 2’s are shown in Figure 5. There is a marginal probability that the distributions for Sy 1’s and Sy 2’s are different at $12 \mu\text{m}$, with the Sy 2’s fainter than the Sy 1’s (7% probability that the difference in the observed distributions occurs due to chance; Table 2), but the distributions are statistically similar at $25 \mu\text{m}$.

We calculate the flux deficit, the fraction of flux “missing” in the IRS aperture relative to IRAS, $F_{def} = (F_{IRAS} - F_{IRS})/F_{IRAS}$. Figures 6 and 7 show that the sample includes some objects for which all the IRAS flux is concentrated within the IRS low-resolution slits (widths $3.5 - 10.5''$), and other objects for which most of the flux falls outside the slit. For most objects, the majority of the IRAS flux is seen by IRS, indicating the surface brightness distributions of the objects are compact. For a few objects, the IRS flux density is higher than the IRAS flux density, suggesting that variability may be contributing to the scatter in the distributions of flux deficit; however, the differences are $\lesssim 20\%$, which is within our flux density uncertainties. These results are consistent with the results of previous studies that compared ground-based photometry of Seyfert galaxies with IRAS photometry. Maiolino et al. (1995) compared $5''$ aperture $10 \mu\text{m}$ flux densities of Seyfert galaxies with the IRAS measurements and showed that the Seyferts displayed a range of ground/IRAS flux densities from $0.0 - 1.0$, indicating that the sources ranged from highly compact objects dominated by the nuclear point source, to those with relatively strong extended emission, associated with star-formation. Gorjian et al. (2004) also compared small aperture ($1.5''$) ground-based photometry of Seyfert galaxies with IRAS measurements. Their results show a similar distribution of flux deficits to our dataset, and these authors note that their data are relatively insensitive to diffuse extended emission due to the high spatial resolution of the detector, and to the small chopping distance used in the observations, which likely resulted in over-subtraction of background emission.

We find that the average flux deficits of Sy 2’s (means of 0.71 and 0.66 at 12 and $25 \mu\text{m}$, respectively) are greater than those of Sy 1’s (means of 0.62 and 0.56; Figures 6 and 7), although statistical comparisons indicate that the differences are only marginally significant (formal probabilities that the parent distributions are the same are $6 - 11\%$; Table 2). The lack of a jump in flux density between the spectra obtained with the SL and LL modules, which have different slit widths, suggests that the emission occurs on scales larger than the LL module slit width ($\sim 10''$). This implies that much of the MIR emission is on kiloparsec scales, and that this difference between

the Sy 1’s and 2’s is related to relatively extended star formation rather than orientation-dependent obscuration in the nucleus. The difference in flux deficits between the Sy 1’s and Sy 2’s implies that the Sy 2’s have *relatively* more extended emission than the Sy 1’s, that is, they are less dominated by the nuclear point source. If both types of Seyfert have the same luminosities, then our results would indicate that the type 2’s have more luminous extended emission than the type 1’s. As noted above, the distributions of nuclear $25\ \mu\text{m}$ flux density for the Sy 1’s and Sy 2’s are similar, while at $12\ \mu\text{m}$ the nuclear flux densities of type 1’s and 2’s are marginally significantly different (Fig. 5 and Table 2). We note that, as the sample was selected at $12\ \mu\text{m}$, Sy 2’s with weak nuclei may have been excluded, resulting in the $12\ \mu\text{m}$ distributions of type 1’s and 2’s appearing more similar than they in fact are; the effects of sample selection on our results are discussed further in §5.3. Therefore it would appear that the Sy 2’s have more extended emission relative to the nuclear emission than the Sy 1’s *and* that the Sy 2’s have, on average, more luminous extended emission than the type 1’s.

4.2. Spectral shapes

We find four distinct types of continuum shapes and spectral features among the Seyfert nuclear spectra. Figure 8 shows typical spectra in each group. An atlas of spectra will be presented when all data have been obtained. All spectra have been converted to the restframe. We group the spectra according to the following main properties:

- Twenty-four objects (47% of the observed objects) have PAH-dominated spectra with strong emission features at 6.2 , $7 - 9$, 11.3 , and $12.9\ \mu\text{m}$ and very red continuum suggestive of cool dust; Mrk 938 is the archetype (Fig. 8). Eight objects, including Mrk 938, show clear silicate absorption at $10\ \mu\text{m}$, while a further eight show possible weak absorption, but the continuum level is difficult to determine due to the strong PAH emission. The remaining 8 objects in this group show no apparent silicate features. There are 5 Sy 1’s, 12 Sy 2’s, 3 LINERs, and 4 starburst galaxies in this group.
- Sixteen objects (31%) have continua that can be described by a broken power-law; they show a flattening in the continuum slope at $\sim 20\ \mu\text{m}$; NGC 4151 is the brightest of this class (Fig. 8). This flattening may be due to a warm ($\sim 170\ \text{K}$) dust component, peaking at $\sim 20\ \mu\text{m}$, dominating the mid-IR emission (e.g., Weedman et al. 2005; Perez Garcia & Rodriguez Espinosa 2001; Rodriguez Espinosa et al. 1996), however, a simple model of an emissivity-weighted blackbody function does not fit the continuum of these spectra well. Models including multiple dust components are required to determine if this is responsible for the continuum shape (Buchanan et al., in prep.). Two of these objects, Mrk6 and Mrk335, show clear silicate emission features (Figure 8b). A further 9 objects in this group, including NGC4151 (Fig. 8), show weak excesses at 10 and $18\ \mu\text{m}$ that may be due to silicate emission; the features are sufficiently weak that a more quantitative analysis is necessary to confirm the presence of silicate dust emission in these spectra. One object, NGC5347, shows apparent weak silicate absorption at $10\ \mu\text{m}$ in its spectrum, while the remaining 4 objects have ambiguous spectral features. There are 9 Sy 1’s, and 7 Sy 2’s in this group. Power-law fits to

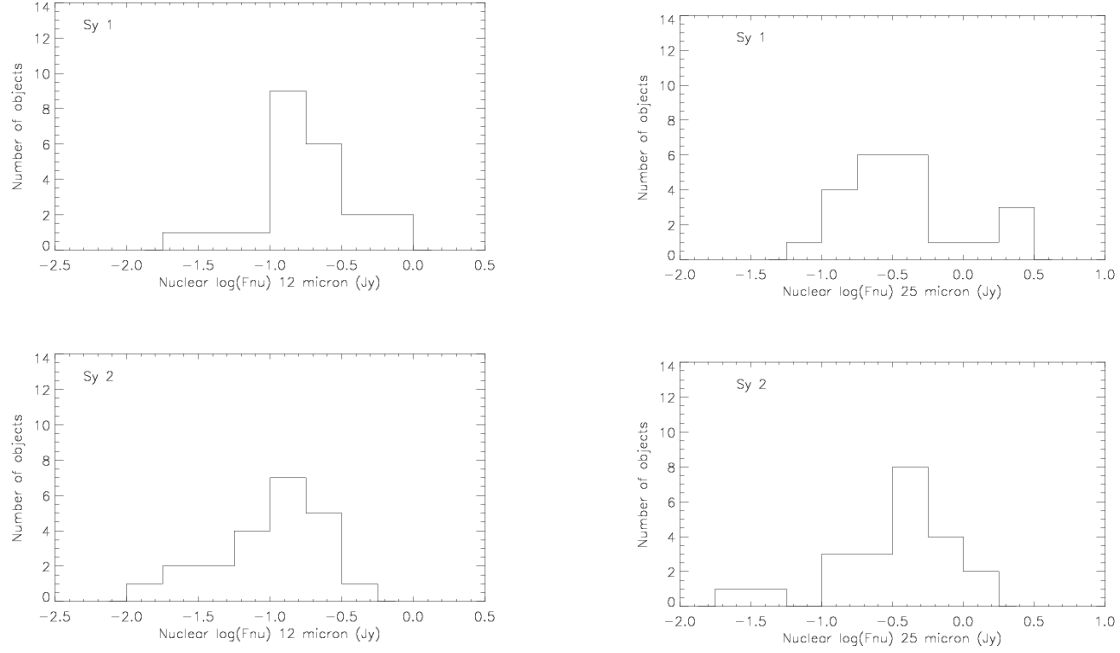


Fig. 5.— Distribution of the 12 μm (*left*) and 25 μm (*right*) nuclear fluxes measured from the IRS spectra. Seyfert 1’s (*top*) and Seyfert 2’s (*bottom*) are shown separately.

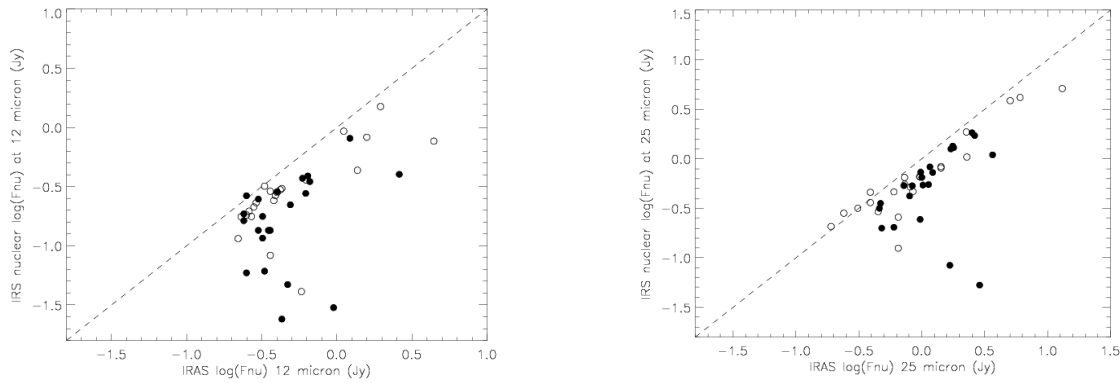


Fig. 6.— IRAS global flux density vs IRS nuclear flux density at 12 μm (*left*) and 25 μm (*right*). Seyfert 1’s (*open circles*) and Seyfert 2’s (*filled circles*) are shown separately. The dashed lines indicate equal global and nuclear fluxes.

Table 2. Properties derived from IRS spectra: results of two-sample tests.

Variable	Group 1	Group 2	Group 1			Group 2		p	p	Figure	
			n_{lim}	Mean	Median	n_{lim}	Mean	Median	(Gehan)		(Logrank)
[1]	[2]	[3]	[4]	[5]	[6]	[7]	[8]	[9]	[10]	[11]	[12]
IRS $\log(F_{12\mu\text{m}})$ (Jy)	obs Sy 1's	obs Sy 2's	0	-0.76	-0.78	0	-0.99	-0.92	0.07	0.07	5
IRS $\log(F_{25\mu\text{m}})$ (Jy)	obs Sy 1's	obs Sy 2's	0	-0.41	-0.47	0	-0.52	-0.47	0.78	0.44	5
12 μm flux deficit	obs Sy 1's	obs Sy 2's	0	0.62	0.57	0	0.71	0.70	0.06	0.11	7
25 μm flux deficit	obs Sy 1's	obs Sy 2's	0	0.56	0.57	0	0.66	0.63	0.06	0.07	7
E/v 1 component	red, PAH	broken P-L	0	14.1	14.1	0	-7.3	-7.3	0.0000	0.0000	13
E/v 1 component	red, PAH	unbroken P-L	0	14.1	14.1	0	-1.1	-2.1	0.0001	0.0000	13
E/v 1 component	broken P-L	unbroken P-L	0	-7.3	-7.3	0	-1.1	-2.1	0.0003	0.0002	13
E/v 1 component	obs Sy 1's	obs Sy 2's	0	-1.2	-2.9	0	6.2	3.3	0.04	0.02	14
$\log(F_{10.6\mu\text{m}}/S_{8.4\text{GHz}})$	obs Sy 1's	obs Sy 2's	5	2.01*	1.91	2	1.16*	1.25	0.002	0.011	16
E/v 1 component	high $L_{8.4\text{GHz}}$	low $L_{8.4\text{GHz}}$	0	5.6	0.7	0	4.7	2.9	0.88	0.59	17

Note. — Generalized Wilcoxon and Logrank two-sample tests were used to determine the probability that the values of the variable (column [1]) in groups 1 and 2 (columns [2] and [3]) were drawn from the same parent distribution. The number of objects in the groups are: all Sy 1's: 37; observed Sy 1's: 22; all Sy 2's: 38; observed Sy 2's: 22. Columns [4]-[6] list the parameters for group 1: the number of limits in the data, the mean value and the median value, derived using the Kaplan-Meier (K-M) estimator where there are limits in the sample. * Indicates the mean is biased because the lower- or uppermost limit was changed to a detection to compute the K-M distribution. Columns [7]-[9] list the same parameters for group 2. Large values of p (columns [10] and [11]) indicate there is no significant difference between the distributions for the two groups. Column [12] refers to the Figure number showing the distribution in the variables.

these spectra indicate that the spectral indices below $20 \mu\text{m}$ range from -2.3 to -0.9, with a median value of $\alpha_{5-20} = -1.3$ (where $S_\nu \propto \nu^\alpha$). The spectral indices above the break are -1.1 – 0.0, with the median $\alpha_{20-35} = -0.4$.

- Eight objects (16%) have power-law continuous spectra over the IRS spectral range $\sim 5 - 35 \mu\text{m}$. NGC 3516 is representative of this class (Fig. 8). These spectra show no strong dust emission or absorption features, though most have weak excesses at 10 and 18 μm that may be due to silicate emission (Fig. 8). Six of these objects are Sy 1’s, and two are Sy 2’s. Power-law fits to these data indicate the spectral indices range from -1.7 to -1.1, with a median of $\alpha_{5-35} = -1.2$.
- Two objects (NGC 1194 & F04385–0828) show a broad absorption feature at 9.7 μm due to silicate dust. NGC 1194 is a Sy 1, and F04385–0828 is a Sy 2.
- One object (NGC 7603) appears to show both PAH and silicate emission features and otherwise fails to meet any of the above classifications. This object is a Sy 1.

The spectral shapes may be quantitatively characterized by the IR colors derived from the spectra. We calculate the spectral index between two wavelengths using

$$\alpha_{2-1} = \log(f_{\lambda_1}/f_{\lambda_2})/\log(\lambda_1/\lambda_2).$$

The spectral index between 20 and 30 μm quantifies the slope of the spectrum (above the $\sim 20 \mu\text{m}$ ‘break’ for broken power-law spectra), while the spectral index between 8 and 10 μm indicates the presence or absence of the 9.7 μm silicate feature and PAH features. The resulting color-color diagrams are given in Figure 9. One Sy 2 (NGC3079) has extreme colors $\alpha_{20-30 \mu\text{m}} = 4.7$ and $\alpha_{8-10 \mu\text{m}} = -12.5$, due to its very red spectrum and strong PAH emission, so it is not shown in Fig. 9. The Sy 1’s (Seyfert types 1.0, 1.2 and 1.5) lie in the lower-right part of the diagram, occupied by unbroken and broken power-law spectra, specifically avoiding the region of the reddest PAH emitters. Sy 2’s are found in both regions. Earlier type Seyferts (i.e. 1 – 1.5) have the bluest colors, while Seyfert 2’s with hidden broad line regions (HBLRs; type 2h) span the range of colors. The fact that Sy 1’s consistently show the bluest infrared colors and the Sy 2’s are the reddest sources indicates the IR spectra are changing systematically with Seyfert type. We consider the implications further in § 5.

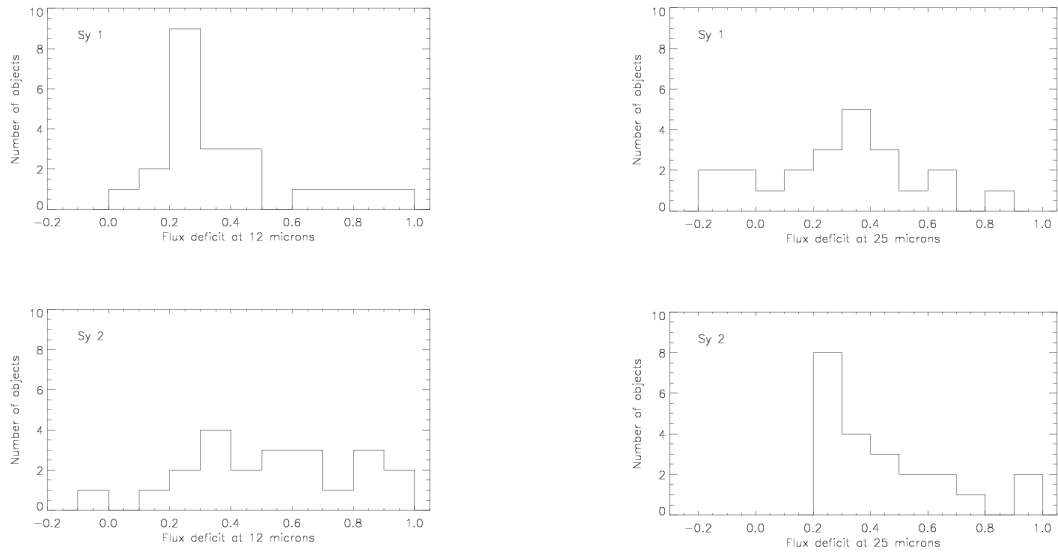


Fig. 7.— Distribution of the flux deficit, the fraction of flux missing in the IRS spectra at $12 \mu\text{m}$ (*left*) and $25 \mu\text{m}$ (*right*) compared with the IRAS flux densities.

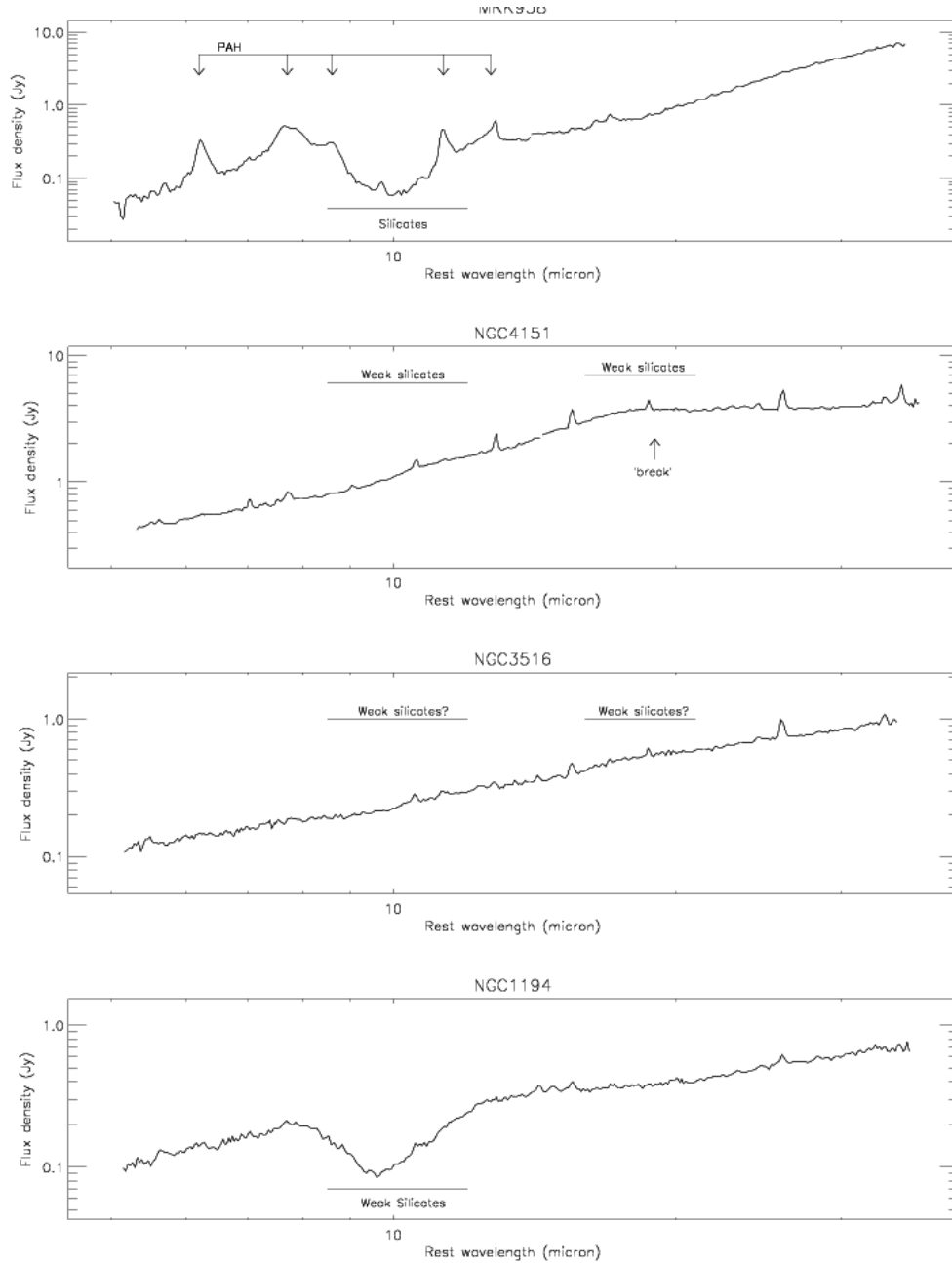


Fig. 8.— (a) Typical spectra in each group: Mrk 938 (red continuum with PAH features), NGC4151 (broken power-law), NGC3516 (power-law), and NGC1194 (silicate absorption). All spectra have been converted to restframe.

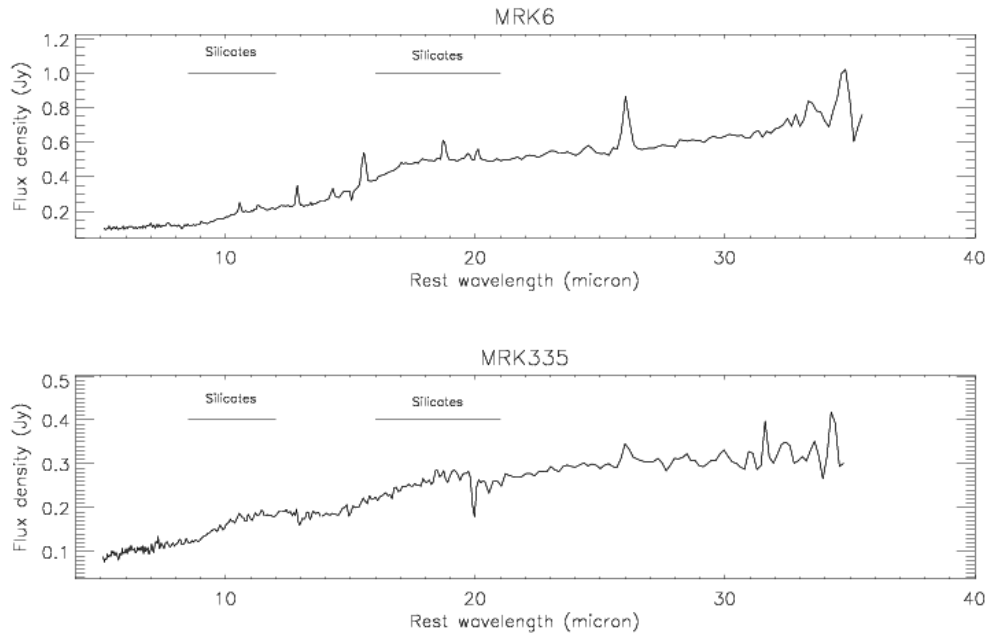


Fig. 8.— (b) The spectra of the two objects, Mrk6 and Mrk335, that show clear silicate emission features at 10 and 18 μm . The spectra have been converted to restframe.

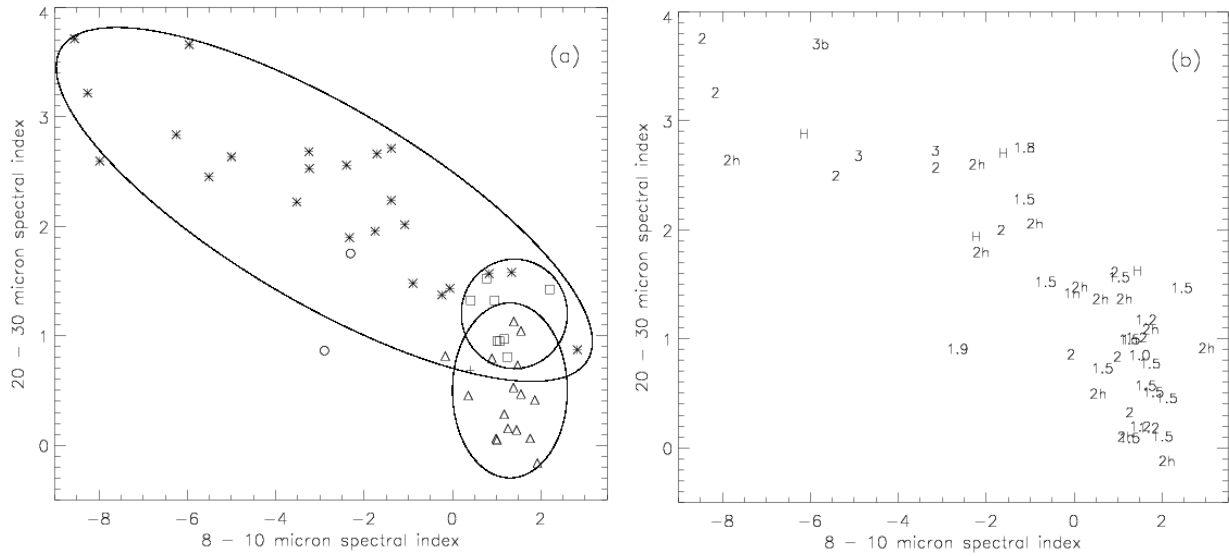


Fig. 9.— IR color-color diagrams derived from the IRS spectra. (a) The symbols indicate the shape of the spectrum: red continuum with PAH features (*stars*), broken power-law (*triangles*), unbroken power-law (*squares*), and silicate absorption (*circles*). The ellipses show the areas occupied by the three largest groups; no ellipse is shown for the 2 objects with silicate absorption. (b) The numbers indicate the Seyfert spectral type. Numbers 1.0 – 1.9 and 1n represent Seyfert 1 subtypes. Symbols 2h and 2 represent Seyfert 2’s with and without HBLRs, respectively. LINERs, with and without broad lines, are shown by numbers 3 and 3b, respectively, and starburst galaxies are indicated by the letter H.

4.3. Principal Component Analysis

We performed a principal component analysis (PCA) on the spectra to determine the component spectral shapes (eigenvectors) producing the variety of spectra seen in the sample (see, e.g., Francis & Wills 1999; Shang & Wills 2004). Because we are presently more interested in the shape of the mid-infrared SED rather than narrow emission features, we median-smoothed all of the spectra to improve the continuous signal in the primary eigenvectors. We adopt a power law spectrum with index $\alpha = -1.2$, (the average slope of the power-law spectra, where $S_\nu \propto \nu^\alpha$) as the AGN ‘mean’ spectrum, rather than using the average spectrum derived from the data, to try to separate this component of the spectra from other features, although using the actual mean spectrum gives similar results. The spectra were converted to the restframe and normalized to unity flux density at $19.0 \mu\text{m}$ before performing the analysis. The PCA computes n eigenvectors, where n is the number of wavelength bins, but for the present data only the first few contribute significantly to the variance. In fact, the first eigenvector is the most dominant and contributes 91% of the variance in the spectra. The first 3 eigenvectors together account for 97.7% of the variance, and the first 6 eigenvectors 99.0%. Figure 10 shows the power law spectrum and the first three eigenvectors.

The first eigenvector shows broad emission features, a deep absorption feature at $\sim 10 \mu\text{m}$, and red continuum above $20 \mu\text{m}$. We interpret the first eigenvector to be dominated by a starburst component, as it closely resembles the spectra of starburst galaxies (Fig. 11). The emission features are attributable to PAH emission, while the absorption feature is due to silicate dust absorption accentuated by the surrounding PAH emission. The change in continuum slope at $\sim 20 \mu\text{m}$ in the PCA eigenvector 1, which is not seen in starburst spectra, probably arises from the broken power-law spectra in the sample, which have negative weights for this eigenvector, and suggests that the first eigenvector does not represent a ‘pure’ starburst. The second eigenvector is dominated by PAH features and so accounts for differing relative strengths of the PAH emission with respect to the silicate absorption in the spectra. The third eigenvector appears to show narrow line emission, in particular [O IV] $\lambda 25.9 \mu\text{m}$, indicating that the smoothing did not completely remove these lines from the spectra.

The individual spectra, or component parts thereof, can be reproduced by summing the ‘mean’ spectrum and the eigenvectors multiplied by their respective weights (e.g., Shang & Wills 2004). The absolute and relative contributions of each eigenvector to each spectrum can be determined using the associated weights. The relative contribution of the first eigenvector to each spectrum appears to be related to the $12 \mu\text{m}$ flux deficit (Figure 12), supporting the conclusion that it predominantly indicates the starburst component of the SED. This figure further suggests that objects with more *extended* starburst activity also have more *nuclear* starburst activity. Figure 13 shows that the relative contribution of eigenvector 1 to each spectrum relates strongly to the shape of the SED, as the different shapes have significantly different contributions from this eigenvector (probabilities $< 0.03\%$ that the distributions are from the same parent distribution, see Table 2). Negative relative contributions indicate that this component is subtracted from the ‘mean’ spectrum to produce the observed spectrum. Negative eigenvector 1 components in broken and unbroken

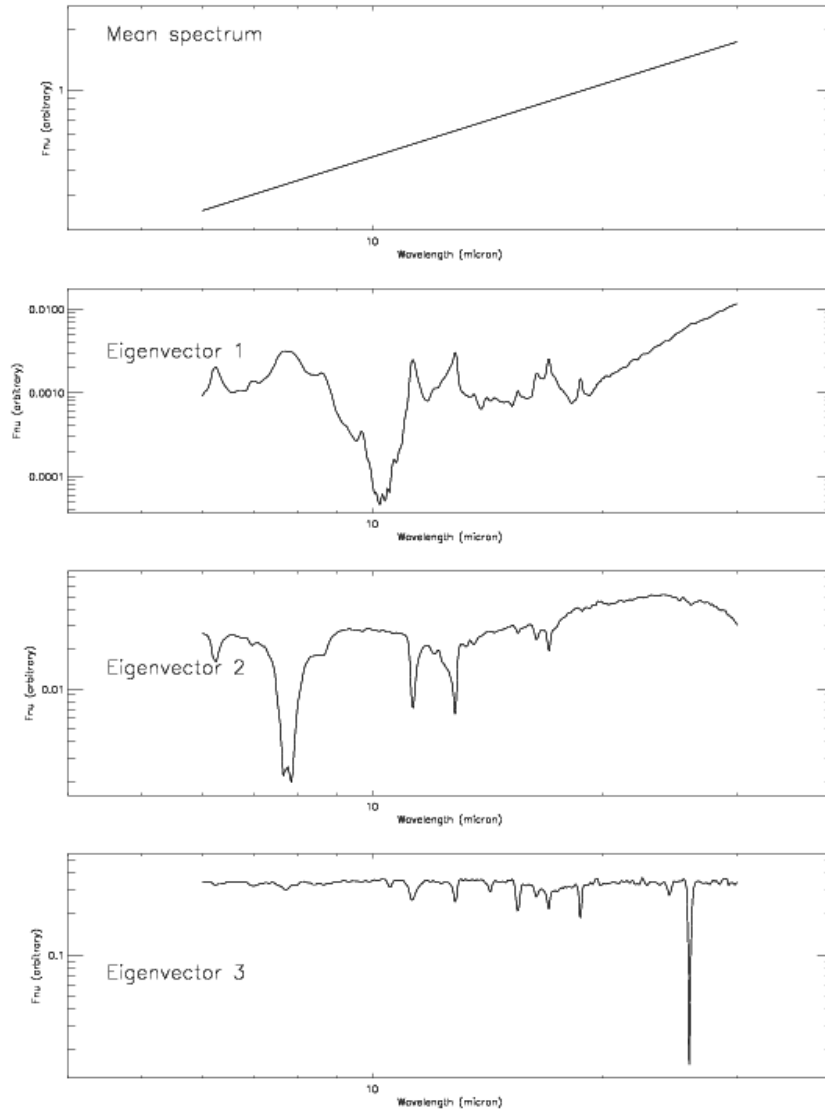


Fig. 10.— The adopted ‘mean AGN’ power-law spectrum (*top*) and first three eigenvectors of the sample of spectra, derived through principal component analysis.

power-law spectra may incorporate $10\ \mu\text{m}$ silicate dust emission. The spectra with red continuum and PAH emission features show the largest eigenvector 1 components, consistent with these objects having the greatest starburst contribution.

The relative contribution of the first eigenvector differs between Seyfert types 1 and 2, with Sy 1's having a negative median component and Sy 2's having a positive median contribution. This supports the result shown in Figure 9 that the spectra showing red continua and PAH emission tend to be Sy 2's while the Sy 1's tend to have other shapes. However, Figure 14 also shows that the Seyfert types have overlapping distributions of the first eigenvector contribution. The differences in the first eigenvector contribution are less significant for Seyfert type 1 than for SED shape. Consistent with this is the lack of separation of Seyfert types in Figure 12. The statistical probabilities determined from two-sample tests are listed in Table 2. We are currently performing radiative transfer modeling of the dust emission in order to determine the physical mechanisms producing the different IR shapes and compare the Seyfert types in more detail (Buchanan et al., in prep).

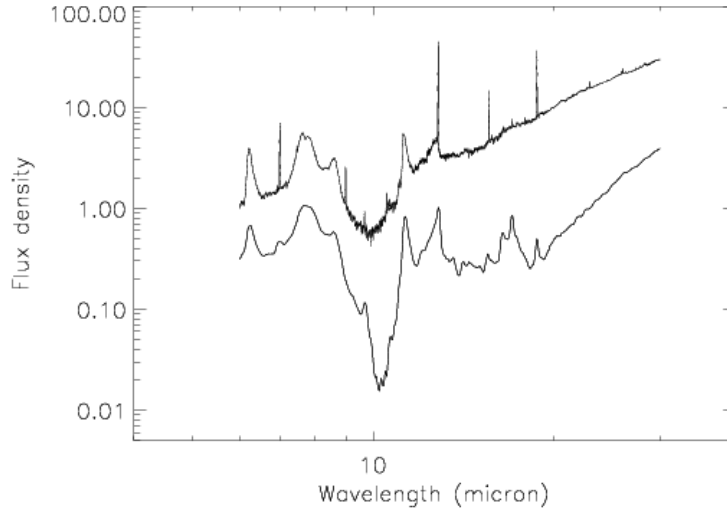


Fig. 11.— The first eigenvector of the PCA which we interpret as dominated by a starburst component but also including contribution from other features (*thin line*), and, for comparison, the ISO spectrum of starburst galaxy M82 (*thick line*). The ISO spectrum was obtained from <http://isc.astro.cornell.edu/sloan/library/swsatlas/atlas.html>. The eigenvector clearly shows the PAH features and silicate absorption seen in starburst galaxies. The shape of the eigenvector at the longer wavelength differs slightly from a starburst shape. It is possible that this shape in the eigenvector produces the break in slope in the NGC 4151-like objects.

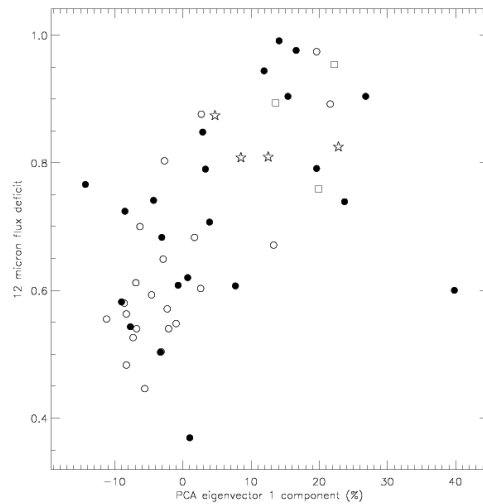


Fig. 12.— The flux deficit at 12 μm (see §4.1) compared with the relative contribution of the first eigenvector derived from the PCA. The symbols indicate the Seyfert type: Sy 1 (*open circles*), Sy 2 (*filled circles*), LINER (*open square*), and starburst galaxy (*open star*).

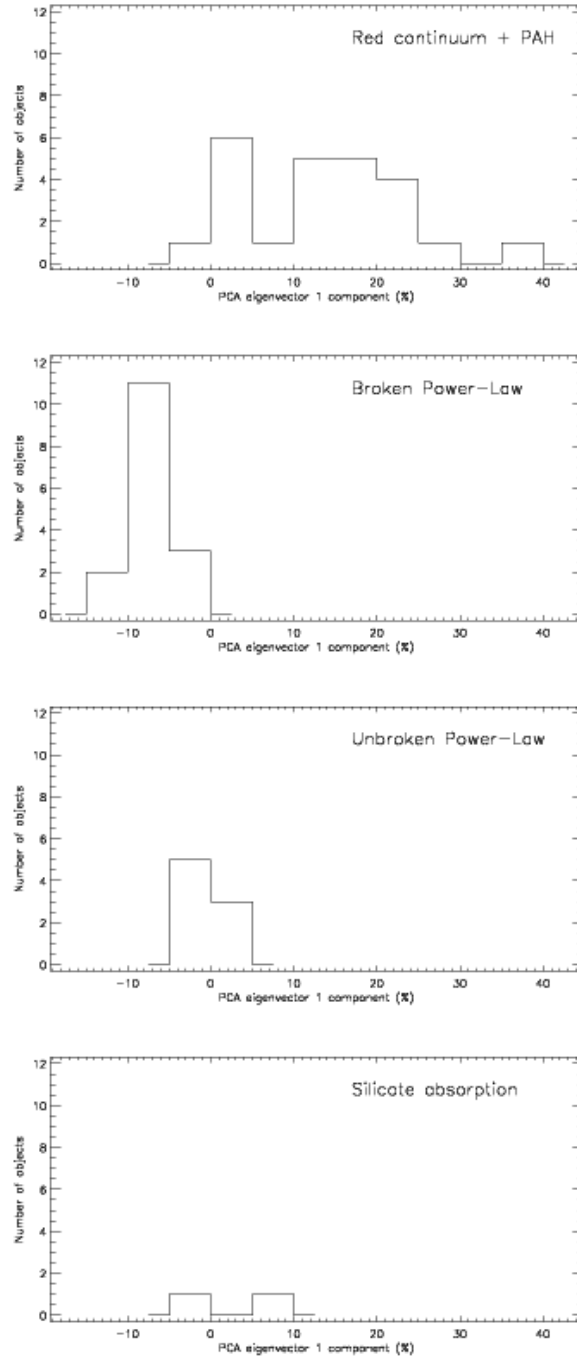


Fig. 13.— Distribution of the relative contribution of eigenvector 1 for the different shapes of the mid-infrared SED in the sample.

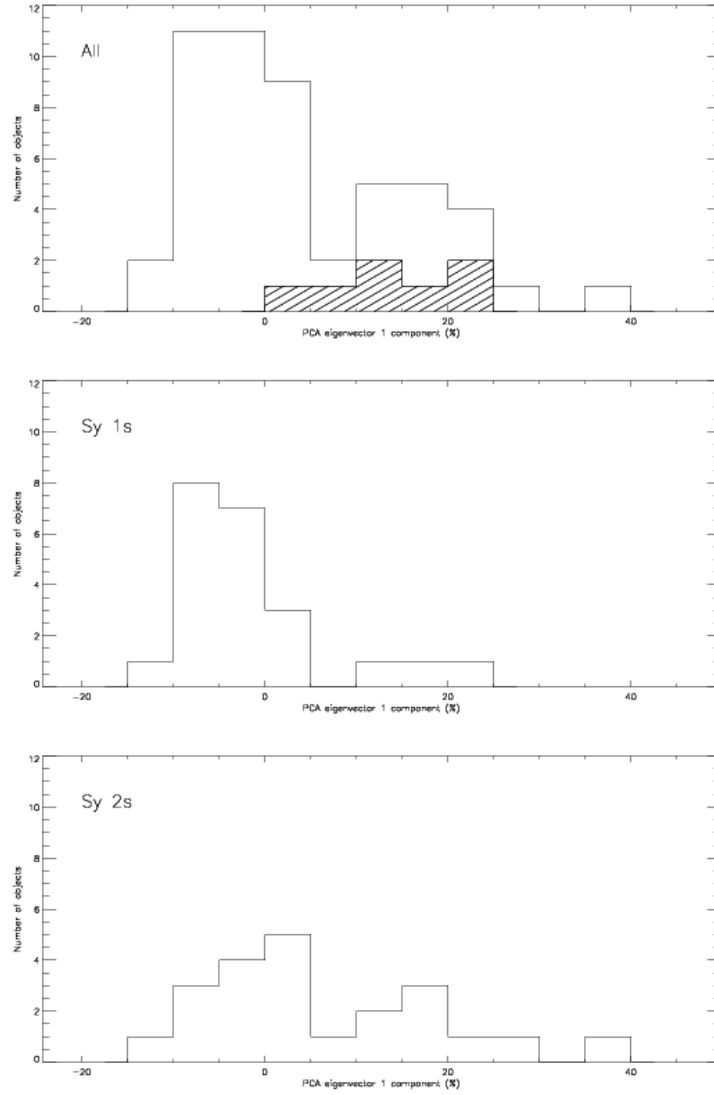


Fig. 14.— Distribution of the relative contribution of eigenvector 1 for all observed objects (*top*), Sy 1's (*middle*) and Sy 2's (*bottom*). The hashed region in the top panel indicates the objects reclassified as non-Seyferts (LINERs and starburst galaxies).

4.4. IR/Radio flux ratios

The unified scheme for active galaxies attributes the differences between Sy 1’s and Sy 2’s to the presence of an optically thick dusty torus surrounding the nucleus (see reviews by Antonucci 1993; Urry & Padovani 1995). Models of such a torus predict that, if the dust is optically thick at mid-IR wavelengths, Sy 1’s (face-on) will be stronger mid-IR emitters than Sy 2’s (edge-on) (Pier & Krolik 1992; Granato & Danese 1994). Heckman (1995) tested this prediction by comparing the mid-IR emission of a heterogeneous sample of Seyfert galaxies. He derived the ratios of $10.6 \mu\text{m}$ to non-thermal radio flux densities, to normalize the IR emission from each object with respect to its intrinsic AGN brightness, and compared the IR/radio flux density ratios of the type 1 and type 2 objects. As noted in §2, the optically thin nuclear radio emission associated with the AGN is isotropic and considered to be representative of the intrinsic AGN power. Heckman (1995) found that Sy 1’s are indeed stronger $10.6 \mu\text{m}$ emitters than Sy 2’s, relative to their isotropic “intrinsic” AGN brightness, by a factor ~ 4 . This result extended the work of Maiolino et al. (1995), who found that the Sy 1’s have brighter absolute nuclear IR emission than Sy 2’s, showing that the difference is due to anisotropy in the mid-IR emission. We derive the nuclear IR to radio flux density ratios of our homogeneous sample of Seyfert galaxies, using our IRS spectra and the nuclear radio flux densities (Fig. 3). Figure 15 shows the distributions of the ratio $S_{10.6 \mu\text{m}}/S_{8.4 \text{GHz}}$ for the Sy 1’s and Sy 2’s. We find the median of the Sy 1’s to be higher than that of the Sy 2’s, by a factor ~ 5 (see Table 2).

We repeated this analysis at intervals of $0.5 - 1.0 \mu\text{m}$ along the IRS spectral range, in order to investigate this difference between Sy 1’s and Sy 2’s across the mid-IR. The median ratio of $\log(S_{\text{IR}}/S_{8.4 \text{GHz}})$ is consistently higher for Sy 1’s than for Sy 2’s at all mid-IR wavelengths (Figure 16), though the statistical significance of the difference decreases at longer wavelengths. The difference between Sy 1’s and 2’s is particularly apparent around $10 \mu\text{m}$. This may be due to strong PAH emission and/or silicate absorption in the Sy 2’s that is absent in the Sy 1’s. Figure 16 shows the ratio of $S_{\text{IR}}/S_{8.4 \text{GHz}}$ of Sy 1’s to that of Sy 2’s. The sharp increase in this ratio towards shorter wavelengths might indicate the presence of a hot dust component, peaking $\sim 2 \mu\text{m}$, in the Sy 1’s that is absent in the Sy 2’s. A higher ratio of IR/radio emission in Sy 1’s is consistent with AGN unification, if the obscuring torus is optically thick in the IR, however a clear separation of the starburst and AGN components in the spectra, from detailed modeling, is necessary before further interpretation of Figure 16 will be possible (see §5.2). In particular, it is unclear if the $10 \mu\text{m}$ peak arises in the torus (Sy 2’s being edge-on) or in the starburst component (preferentially stronger in Sy 2’s).

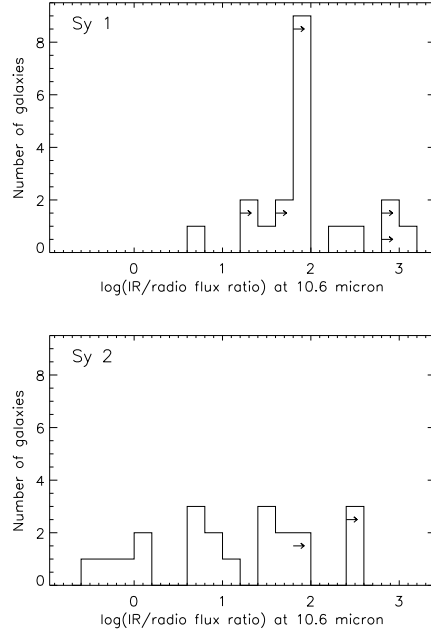


Fig. 15.— Histograms of the 10.6 μm to 8.4 GHz flux density ratio for the Sy 1’s (*top*) and Sy 2’s (*bottom*). Lower limits (sources where the radio flux is an upper limit) are indicated by arrows.

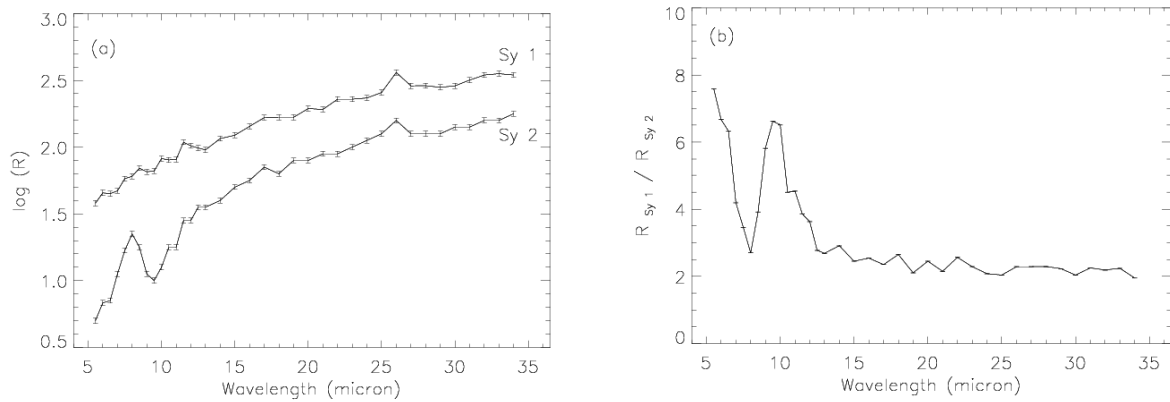


Fig. 16.— (a) Logarithmic ratio $\log(R)$, where $R = \text{median IR/radio flux density ratio}$, of the Sy 1’s and Sy 2’s, as a function of the IR wavelength. (b) The ratio of R for Sy 1’s to that of Sy 2’s at each IR wavelength.

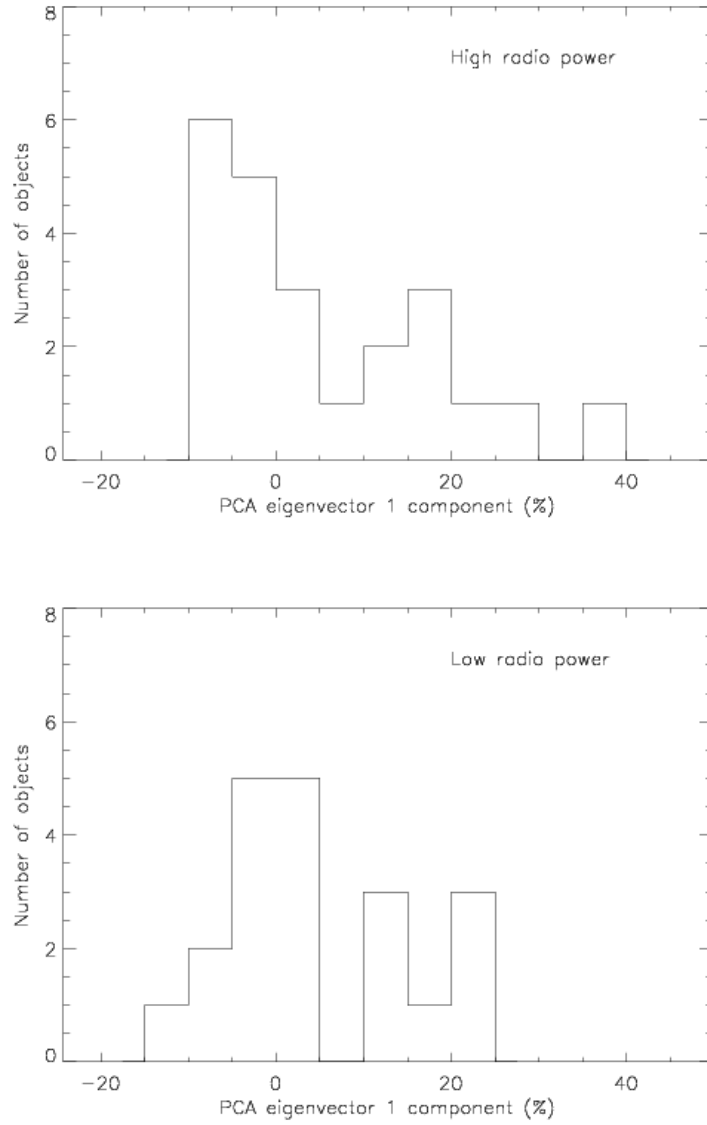


Fig. 17.— Distribution of the relative contributions of eigenvector 1 for high (*top*) and low (*bottom*) radio power sources, separated by the median radio power of $2.2 \times 10^{21} \text{ W Hz}^{-1}$.

5. Discussion

We now consider the implications of our results for our understanding of the starburst/AGN connection, the AGN unified model, and selection effects in AGN samples.

5.1. The relative IR contributions of starburst and AGN

Spitzer spectra of the sample reveal distinct continuum shapes and dust features. The similarity in the features between the red objects like MRK 938 (see Fig. 8) and the IR spectra of starburst galaxies such as M 82 (see Fig. 11) strongly suggests these objects are dominated by the starburst contribution to the dust heating at mid-infrared wavelengths. We find no difference in the redshifts of these objects compared with the other IR spectral types, indicating that the relative strength of the starburst component is not an aperture effect. We do find evidence, however, that the strength of the nuclear starburst, as measured by the contribution of the first eigenvector in the PCA, is related to the extended star formation, measured by the $12\ \mu\text{m}$ flux deficit (Figure 12). In the starburst-dominated objects the dust is cool and so peaks longward of $30\ \mu\text{m}$, and the PAH features are strong. In contrast, objects with broken and unbroken power-law spectra are probably dominated by the AGN contribution to the spectrum. Previous studies suggest that this AGN contribution is a warm dust component (e.g., Rieke 1978; McAlary & Rieke 1988; Barvainis 1987; Pier & Krolik 1993; Polletta et al. 2000). It is possible that the power-law spectra are produced by dust with a range of temperatures (Panagia & Felli 1975), and the apparent break in the broken power-law spectra is produced by a dominant dust component peaking at $\sim 20\ \mu\text{m}$. MFIR photometric SEDs of several Seyferts, based on *ISO* data, are consistent with such a dust component (Rodríguez Espinosa et al. 1996; Pérez García & Rodríguez Espinosa 2001). That the mid-IR emission is dominated by dust is also supported by the recent identification of silicate dust emission features in AGN mid-IR spectra (Weedman et al. 2005; Hao et al. 2005c; Siebenmorgen et al. 2005). In order to understand the spectral shapes, we have begun comprehensive modeling using both AGN and starburst dust radiative transfer models, the results of which will be reported elsewhere (Buchanan et al., in prep.). The sharpness of the break in some IRS spectra near $20\ \mu\text{m}$ (e.g., NGC 4151; Fig. 8) is difficult to reproduce using simple dust models, however, even with several dust components. The IR emission is clearly produced by dust emission in the two objects with strong silicate absorption at $10\ \mu\text{m}$.

An alternative possibility is that the infrared emission may be non-thermal in origin, such as synchrotron emission. The broad-band photometric SEDs of nearby Seyfert galaxies provide evidence that the mid-IR emission of many Sy 1's is predominantly non-thermal (Edelson, Malkan, & Rieke 1987; Ward et al. 1987; Carleton et al. 1987), although a non-thermal IR component is not always necessary to model AGN SEDs (Barvainis 1990). The detection of rapid variability at $10\ \mu\text{m}$ in some nearby quasars indicates a non-thermal component of the mid-IR emission (Neugebauer & Matthews 1999), and further supports that the Sy 1's may also have a non-thermal IR contribution.

Comparison of the IR and nuclear 8.4 GHz radio flux densities suggests that the infrared emission is not a continuation of the radio synchrotron spectrum, as the IR fluxes are at least an order of magnitude too high. If the synchrotron were self-absorbed and the spectral turnover occurred at 20 μm , consistent with the observed break in the power-law spectra, the component would have to be $\lesssim 10^{11}$ m in size, on the same scale as the accretion disk (Urry & Padovani 1995). The typical spectral slope at frequencies below (i.e., wavelengths above 20 μm) the turnover would have to be 0.8 to match the radio flux densities. This slope, and the typical slopes at frequencies above the turnover (wavelengths below 20 μm) of ~ -1.3 , are not inconsistent with self-absorbed synchrotron emission, so we cannot rule this out as the origin of the power-law spectra. However, the energy density of such a synchrotron component would be very large ($\sim 9 \times 10^8 \text{ erg cm}^{-3}$), so extreme conditions would be required to confine it. The total energy in the plasma would also be large, ($\sim 10^{40}$ ergs), suggesting that such a component is unlikely.

A third alternative for the broken and unbroken power-law spectra is free-free bremsstrahlung, however this would produce a much flatter slope ($S_\nu \propto \nu^{-0.4}$) (Barvainis 1993) than is observed in the spectra.

A final possibility is that the IR emission is a continuation of the accretion disk spectrum, with a slope of, for example, 1/3 (Eq. 5.46, p.92; Frank, King, & Raine 1992), though more realistic accretion models will modify this (e.g., Litchfield et al. 1989). This will be investigated in the future using X-ray – optical data in conjunction with the IR data.

The results of our principal component analysis show that the first eigenvector produces more than 90% of the variance in the observed spectral shapes and is dominated by a starburst spectral shape. This suggests that the relative contribution of star-formation to the IR spectrum is an important factor determining the observed spectral shape. However, we emphasize that, while the starburst contribution dominates the observed differences in the IR spectral shapes, the starburst component does not dominate the total emission of each object. Most spectra are comprised of a power law plus a <20% contribution of eigenvector 1 (Figure 14). We found a significant difference between the contribution of the first eigenvector to the spectra of the Sy 1’s and Sy 2’s. This is consistent with the (on average) higher flux deficits at 12 and 25 μm in Sy 2’s compared with Sy 1’s, suggesting that extended flux (i.e., associated with circumnuclear star formation) contributes more to the total mid-IR flux in Sy 2’s than Sy 1’s. Our results confirm the finding of Maiolino et al. (1995), based on ground-based photometry, that Sy 2’s show more extended star formation than Sy 1’s. The sample of objects studied by Maiolino et al. (1995) were optically selected, and therefore our result is not due to an infrared selection bias. We have concluded that the extended emission is associated with star formation, however it has also been shown that extended IR emission, on scales of tens of parsecs, can also be associated with the AGN (e.g., Mason et al. 2006; Bock et al. 1998). Our data demonstrates a clear relationship between the Seyfert type and the IR SED shape (i.e., Sy 1’s tend to have power-law or broken power-law SEDs and Sy 2’s have greater starburst contribution to their SEDs), but there is not a 1-to-1 correspondence between the optical Seyfert type and the IR spectral shape. It is clear that star formation and complex dust obscuration play

key roles in producing the observed variety of spectral shapes in the IRS spectra. Homogeneous optical spectra, to ensure uniform Seyfert classifications, and simultaneous modeling of the optical and IR SEDs are necessary to elucidate these relations.

5.2. Properties of the obscuring medium (comparison with torus models)

Comparing the optical spectral types of the IR spectral groups (§4.2), it is not immediately apparent whether or not the IR spectra support orientation-dependent obscuration. Torus models predict silicate emission in type 1 (face-on) objects and silicate absorption features in type 2 (edge-on) objects (Rowan-Robinson & Crawford 1989; Pier & Krolik 1992; Siebenmorgen et al. 2004, though see also Nenkova et al. 2002). We would expect edge-on objects to show the most dust absorption. The two objects that show strong silicate absorption have optical spectral types Sy 1.9 and HBLR Sy 2, which is not inconsistent with the unified scheme. The majority of broken power-law spectra that may show silicate emission features are Sy 1.2 and Sy 1.5, although the group includes several Sy 2’s as well. The relative contribution of a starburst to the IR spectrum appears to be greater in Sy 2’s, possibly due to a selection effect (see §5.3), so that it is difficult to discern any orientation-dependent difference in the AGN component of the spectra.

The ratio of IR to radio flux densities is consistently higher for the type 1 objects in our sample than the type 2 objects, at all observed wavelengths. Interpreting this in the context of the unified scheme, this may indicate that the obscuring material is optically thick up to at least $30 \mu\text{m}$. However, optically thick smooth-density torus models predict much larger differences between the face-on and edge-on Seyferts than the observed factor of ~ 2 , seen in our data at wavelengths longer than $\sim 15 \mu\text{m}$ (Figure 16). For example, Pier & Krolik (1992) show that, for an optically thick torus, the face-on objects are expected to be at least a factor of 5 and up to several orders of magnitude brighter than the edge-on objects. Lutz et al. (2004) first noted that torus models cannot explain the observed lack of anisotropy in the IR emission of Seyferts, when they compared the $6 \mu\text{m}$ emission of Sy 1’s and 2’s, normalized to the intrinsic hard X-ray emission. Our findings, while not identical to those of Lutz et al. (2004) at $6 \mu\text{m}$ (discussed below), confirm that observational data do not match the predictions of optically thick smooth-density torus models.

Our results are consistent with the torus becoming optically *thin* in the mid-IR, at around $15 \mu\text{m}$. However, a mid-IR optical depth < 1 would imply column density $< 10^{23} \text{ cm}^{-2}$ (e.g., Lutz et al. 2004), which is inconsistent with X-ray observations of many Seyfert 2 galaxies (e.g., Bassani et al. 1999). The observed high X-ray column densities of Sy 2’s could be reconciled with optically thin IR emission, if the X-ray absorption is dominated by gas in which the dust has been destroyed, e.g., close to the nucleus within the dust sublimation radius. There is some evidence that this may be possible: variability in the X-ray column densities of two Seyfert 2’s on timescales of less than a day indicates that absorbing columns of up to $5 \times 10^{23} \text{ cm}^{-2}$ exist on scales of less than a few hundred Schwarzschild radii (Risaliti et al. 2005; Elvis et al. 2004). Thus our IR/radio flux density ratios could indicate that the torus is optically thin above $15 \mu\text{m}$. As noted in §4.4 the difference in

the ratio of IR/radio flux densities between Sy 1’s and Sy 2’s is particularly apparent around $10\ \mu\text{m}$; the $10\ \mu\text{m}$ flux density from an optically thin torus is predicted to show more anisotropy than the surrounding continuum (Pier & Krolik 1992), suggesting that our results are also consistent with an optically thin torus at shorter mid-IR wavelengths than $15\ \mu\text{m}$. However, it is not clear whether the $6.2\ \mu\text{m}$ PAH feature associated with star formation is contributing to the apparent peak at $10\ \mu\text{m}$ in Figure 16(b). Certainly, the steep rise in this figure towards the shortest wavelengths (from 7 down to $5\ \mu\text{m}$) suggests that the obscuring material is optically thick at these wavelengths.

Clumpy torus models can accommodate much less anisotropy of the mid-IR emission than models with smooth radial density distributions (e.g., Nenkova et al. 2002). The torus emitting near-isotropically in the mid-IR, but with anisotropic X-ray absorption, can be explained by clumpy torus models, if the radial distribution of optically thick dust clumps is steep (Nenkova et al. 2006, in preparation). The similar ratios of IR/radio flux density of Sy 1’s and Sy 2’s observed in our sample therefore may be explained by an optically thick clumpy torus.

Our IR/radio ratios at $6\ \mu\text{m}$ appear to be in disagreement with those of Lutz et al. (2004), who found no significant difference between Sy 1’s and Sy 2’s in their ratio of X-ray/IR flux densities. These authors used the intrinsic (i.e., absorption-corrected) X-ray flux densities as a measure of the AGN luminosity, and determined the ratio of the X-ray flux density to the $6\ \mu\text{m}$ AGN continuum flux density, derived from ISO spectra. Lutz et al. (2004) find the average X-ray/IR flux ratio of Sy 1’s in their sample to be a factor of ~ 2 less than the average ratio for type 2 Seyferts, which is contrary to the expectations of torus models in the unified scheme. Our results show a factor of ~ 7 difference at this wavelength (Fig. 16), in the opposite direction. There are several factors which are likely to contribute to the disagreement between our results and those of Lutz et al. (2004). Firstly, the relative AGN and starburst contributions to the IR flux densities are likely to be different in the two studies. The ISO data of Lutz et al. (2004) were obtained using a $24''$ aperture, which will include a large contribution of extended emission; the authors account for this using spectral decomposition to determine the AGN continuum. In contrast our data are relatively small aperture and so better isolate the nuclear emission, but we have not attempted to remove the starburst contribution to the IR emission, which is clearly different for the type 1’s and 2’s in our sample. Secondly, the sample studied by Lutz et al. (2004) was heterogeneous and includes, for example, Sy 1’s and Sy 2’s with different distance and intrinsic luminosity distributions. The redshift and intrinsic (radio) luminosity distributions of the type 1’s and 2’s in our homogeneous sample are similar (see §2) and so will not have biased the comparison of the mid-IR emission. Finally, the studies are using measurements at different wavelengths to represent the intrinsic AGN luminosities. Large corrections (up to an order of magnitude) are required to determine the intrinsic X-ray flux densities from the observed flux densities, and therefore there may be considerable uncertainty in the obtained intrinsic AGN luminosities, although we note that Lutz et al. (2004) find no evidence for a systematic offset in the absorption-corrected values which would bias their result. Given the various systematic biases in each of the studies, it is perhaps not surprising that the exact ratios of Sy 1/Sy 2/ IR emission measured are not the same. However,

despite this disagreement, our results at the longer wavelengths lead us to the same conclusion as Lutz et al. (2004): the data are not consistent with optically thick, smooth-density torus models (e.g, Efstathiou & Rowan-Robinson 1995), which predict strongly anisotropic mid-IR emission.

5.3. Selection effects in the IR

In the context of the unified scheme, the IR/radio flux density ratios of the Sy 1’s and Sy 2’s in our sample suggest that the torus may be optically thick at wavelengths shorter than $\sim 15 \mu\text{m}$ (see Figure 16 and §5.2). The Seyfert sample was selected using IRAS fluxes at $12 \mu\text{m}$, therefore we might expect there to be orientation-dependent selection effects biasing our sample, that is, that dust obscuration will bias the sample towards type 1’s. A second possible selection effect, if Sy 2’s have more star formation than Sy 1’s, is discussed below. To fall above the flux limit of the sample, the Sy 2’s must contain intrinsically brighter AGNs than the Sy 1’s, because the Sy 2’s suffer more MIR dust obscuration. However, we find no significant difference between the AGN luminosities of the Sy 1’s and Sy 2’s in the sample (as measured by the optically thin radio emission, see §2). Further, if the Sy 2’s have more luminous AGN emission than the Sy 1’s due to a selection effect, we may expect that the contribution of the first eigenvector would be different for high and low radio power sources. Again, we find no significant difference in the distributions of relative eigenvector 1 components for high ($> 10^{24} \text{ W Hz}^{-1}$) and low power radio sources in the sample (Figure 17). It is possible that small number statistics are preventing us from detecting a significant difference in the radio powers of the Sy 1’s and 2’s (see Table 1). The lower IR/radio flux density ratios observed in Sy 2’s compared with Sy 1’s are consistent with more luminous radio sources in Sy 1’s.

A second selection effect could be operating in the opposite direction to that associated with orientation-dependent obscuration of the nucleus. Sy 2’s with intrinsically faint nuclei could make it into the sample if they have an additional starburst contribution to the $12 \mu\text{m}$ flux density. This would result in the sample being biased towards Sy 2’s with a greater relative and absolute starburst contribution than the Sy 1’s in the sample. It is clear from our color-color diagram (Fig. 9) and principal component analysis that the observed Sy 2’s show a stronger starburst contribution to their infrared spectra than the Sy 1’s, consistent with such a bias. A near-infrared study has shown that the Sy 2’s in the $12 \mu\text{m}$ sample are not biased towards those with powerful nuclear starbursts compared with optically-selected Sy 2’s (Imanishi & Alonso-Herrero 2004), but the $12 \mu\text{m}$ -selected Sy 2’s may be biased towards more luminous *extended* starbursts due to the large-aperture IRAS observations used to select them.

Thus we cannot exclude the possibility that the two selection effects described above are canceling each other out to give the same distribution of infrared luminosities for Sy 1’s and 2’s. However, it is puzzling that, if the sample is biased towards Sy 2’s with intrinsically brighter AGN and/or those with greater starburst contribution to their IR emission, that we see no differences in the AGN (radio) luminosities. The similar distribution of intrinsic AGN luminosities (radio powers) may imply that the effects of obscuration and starburst contribution are small compared with the

AGN luminosities. Alternatively, the statistical results may become clearer when more of our data are available. Further leverage on selection effects and biases can be obtained using IRAC imaging data, which we will address in future work.

The selection of Seyfert samples based on the isotropic luminosity of the AGN and which are unbiased with respect to orientation is essential to study the physics of active galaxies and the AGN/starburst connection. An unbiased sample is difficult to obtain, however. The optical and 0.1 – 10 keV X-ray continuum fluxes suffer uncertain orientation dependent obscuration so favor Sy 1’s and discriminate against Sy 2’s (e.g., Green, Schmidt & Liebert 1987; Heckman et al. 1995). Optical line emission, such as [O III] λ 5007, originates in the narrow line region so should be isotropic and representative of the intrinsic AGN luminosity. However it has been shown recently (Hao et al. 2005b) that, while the numbers of 1’s and 2’s are comparable at low [O III] luminosity, Seyfert 1’s outnumber the 2’s by a factor of about 3 at high [O III] luminosity, suggesting that [O III] luminosity may not be an unbiased criterion. It has further been argued, for powerful AGN, that some [O III] emission may come from within the torus, and therefore be orientation-dependent (di Serego Alighieri et al. 1997). Spinoglio & Malkan (1989) argued that selection effects are minimal in the 7 – 12 μ m region. The extended 12 μ m sample of Seyfert galaxies was thus selected to minimize wavelength-dependent selection effects. Our results have shown, however, that the nuclear obscuring material may be optically thick at MIR wavelengths up to 15 μ m and so selection effects are still important in the mid-IR. The torus presumably becomes optically thin at far-IR wavelengths, but at these wavelengths it becomes difficult to separate nuclear emission from circumnuclear star formation, which emits strongly at FIR wavelengths due to the presence of cold dust. Similarly, at low radio frequencies and spatial resolutions, such as the FIRST survey at 1.4 GHz (White et al. 1997), the relatively strong contribution of star formation to the nuclear spectrum may bias the selection. To obtain a sample of Seyfert galaxies unbiased by possible orientation effects, it is therefore necessary to select galaxies based on optically thin, compact radio emission associated with the active nucleus (e.g., Thean et al. 2001). A large area (10 square degrees), sensitive (0.2 mJy/beam) survey at high spatial resolution (0.2 ″) at high frequency (8 GHz) would seem to be a useful way to select nearby Sy 1’s and Sy 2’s unbiased by orientation effects.

6. Conclusions

We present the results of Spitzer IRS nuclear spectra for the first 51 of a complete sample of 12 μ m selected Seyfert galaxies. We find the following main conclusions:

- The spectra clearly divide into groups based on their continuum shapes and spectral features. The largest group (47% of the sample of 51) shows very red continuum suggestive of cool dust and strong emission features attributed to PAHs. Sixteen objects (31%) have a power-law continuum with spectral indices $\alpha_{5-20\mu\text{m}} = -2.3 - -0.9$ that flatten to $\alpha_{20-35\mu\text{m}} = -1.1 - 0.0$ at $\sim 20\mu\text{m}$. Clear silicate emission features at 10 and 18 μ m are found in two of these objects (Mrk 6 and Mrk 335). A further 16% of the sample show power-law continua with unchanging slopes of $\alpha_{5-35\mu\text{m}} = -1.7$

– -1.1. Two objects are dominated by a broad silicate absorption feature. One object in the sample shows an unusual spectrum dominated by emission features, that is unlike any of the other spectra. Some features are clearly related to the starburst contribution to the IR spectrum, while the mechanisms producing the power-law continuum attributed to the AGN component are not yet clear. The precise correspondence between the IR types and the optical spectral types is unclear, firstly because the exact contributions of the AGN and starburst to the IR emission are not clearly separated by colors or principal component analysis, and secondly because the Seyfert types are heterogeneous and often ambiguous.

- Principal component analysis suggests that the relative contribution of starburst-heated dust emission to the SED is the dominant cause of variance in the observed spectra, although all the spectra are dominated by a power-law component. The close detailed agreement of eigenvector 1 with the spectrum of a starburst at $\lambda < 20 \mu\text{m}$ makes it almost certain that eigenvector 1 is tracking the starburst component in these AGNs. Moreover, that eigenvector 1 is linked to $12 \mu\text{m}$ IRAS/Spitzer flux deficit, shows that this star formation is extended and so not a purely nuclear phenomenon.

- We find that the Sy 2's typically show stronger starburst contributions in their IR spectra than the Sy 1's, confirming previous results found using photometric data. This result is in disagreement with the predictions of unified schemes. The stronger starburst contribution in Sy 2's compared with Sy 1's may be a selection effect in our sample, though we find no evidence supporting the presence of a bias in our sample.

- We confirm the previous finding that Sy 1's show higher ratios of IR/radio emission than Sy 2's at $\sim 10 \mu\text{m}$, by a factor > 6 , however we find that the difference between type 1's and 2's decreases to a factor of ~ 2 beyond $\sim 15 \mu\text{m}$. In the context of unified schemes, this presents a challenge for dusty torus models, which generally predict much larger anisotropy. The observed factor of ~ 2 difference between the type 1's and 2's in their IR/radio ratios above $15 \mu\text{m}$ requires the standard smooth-density torus models to be optically thin at these wavelengths. However, the resulting low torus opacity requires that the high observed columns detected in X-ray absorption be produced in gas with very low dust to gas ratio (perhaps within the dust sublimation region). On the other hand, our observations may be consistent with clumpy torus models (e.g., Nenkova et al. 2002) containing a steep radial distribution of optically thick dense clumps.

- The selection of our sample at $12 \mu\text{m}$, where the torus may be optically thick, implies there may be orientation-dependent biases in the sample, however we see no evidence for these in our results. Detailed modeling of the continuum emission is underway to separate in detail the starburst and AGN contributions to the IR spectrum in order to place constraints on the opacity and geometry of the nuclear obscuring material, and to compare the relative starburst contributions of Seyfert types 1 and 2.

We thank the referee for a careful reading of the manuscript, which resulted in significant improvements to the paper. This work is based on observations made with the Spitzer Space Telescope, which is operated by the Jet Propulsion Laboratory, California Institute of Technology

under a contract with NASA. Support for this work was provided by NASA through an award issued by JPL/Caltech. The IRS was a collaborative venture between Cornell University and Ball Aerospace Corporation funded by NASA through the Jet Propulsion Laboratory and Ames Research Center. SMART was developed by the IRS Team at Cornell University and is available through the Spitzer Science Center at Caltech. This research has made use of NASA's Astrophysics Data System.

Facilities: Spitzer

REFERENCES

- Antonucci, R. 1993, *ARA&A*, 31, 473
- Barvainis, R. 1987, *ApJ*, 320, 537
- Barvainis, R. 1990, *ApJ*, 353, 419
- Barvainis, R. 1993, *ApJ*, 412, 513
- Bassani, L., Dadina, M., Maiolino, R., Salvati, M., Risaliti, G., della Ceca, R., Matt, G., & Zamorani, G. 1999, *ApJS*, 121, 473
- Bock, J. J., Marsh, K. A., Ressler, M. E., & Werner, M. W. 1998, *ApJ*, 504, L5
- Carleton, N. P., Elvis, M., Fabbiano, G., Willner, S. P., Lawrence, A., & Ward, M. 1987, *ApJ*, 318, 595
- di Serego Alighieri, S., Cimatti, A., Fosbury, R. A. E., & Hes, R. 1997, *A&A*, 328, 510
- Edelson, R. A. 1987, *ApJ*, 313, 651
- Edelson, R. A., Malkan, M. A., & Rieke, G. H. 1987, *ApJ*, 321, 233
- Efstathiou, A., & Rowan-Robinson, M. 1995, *MNRAS*, 273, 649
- Elvis, M., Risaliti, G., Nicastro, F., Miller, J. M., Fiore, F., & Puccetti, S. 2004, *ApJ*, 615, L25
- Feigelson, E. D., & Nelson, P. I. 1985, *ApJ*, 293, 192
- Francis, P. J., & Wills, B. J. 1999, *ASP Conf. Ser.* 162: Quasars and Cosmology, 162, 363
- Frank, J., King, A. R., & Raine, D. J. 1992, *Accretion power in astrophysics* (2nd ed.; Cambridge: CUP)
- Gallimore, J. F., Baum, S. A., O'Dea, C. P., Pedlar, A., & Brinks, E. 1999, *ApJ*, 524, 684
- Gebhardt, K., et al. 2000, *ApJ*, 539, L13
- Giuricin, G., Mardirossian, F., Mezzetti, M., & Bertotti, G. 1990, *ApJS*, 72, 551
- Gorjian, et al. 2004, *ApJ*, 605, 156
- Granato, G. L., & Danese, L. 1994, *MNRAS*, 268, 235
- Green, R. F., Schmidt, M., & Liebert, J., 1987, *ApJS*, 61, 305
- Hao, L., et al. 2005a, *AJ*, 129, 1783
- Hao, L., et al. 2005b, *AJ*, 129, 1795
- Hao, L., Spoon, H. W. W., Sloan, G. C., Marshall, J. A., Armus, L., Tielens, A. G. G. M., Sargent, B., van Bemmell, I. M., Charmandaris, V., Weedman, D. W., Houck, J. R. 2005c, *astro-ph/0504423*
- Heckman, T. M. 1995, *ApJ*, 446, 101
- Heckman, T., et al. 1995, *ApJ*, 452, 549
- Higdon, S. J. U. et al. 2004, *PASP*, 116, 975
- Ho, L. C., Filippenko, A. V., & Sargent, W. L. W. 1997, *ApJS*, 112, 315
- Houck, J. R., et al. 2004, *ApJS*, 154, 18
- Imanishi, M., & Alonso-Herrero, A. 2004, *ApJ*, 614, 122
- Ivezic, Z., & Elitzur, M. 1997, *MNRAS*, 287, 799
- Jaffe, W., et al. 2004, *Nature*, 429, 47

- Jogee, S., Scoville, N., & Kenney, J. D. P. 2005, *ApJ*, 630, 837
- Kauffmann, G., et al. 2003, *MNRAS*, 346, 1055
- Krolik, J. H., & Begelman, M. C. 1988, *ApJ*, 329, 702
- Kukula, M. J., Pedlar, A., Baum, S. A., & O’Dea, C. P. 1995, *MNRAS*, 276, 1262
- Lavalley, M., Isobe, T., & Feigelson, E. 1992, *ASP Conf. Ser.* 25: *Astronomical Data Analysis Software and Systems I*, 25, 245
- Litchfield, S. J., King, A. R., & Brooker, J. R. E. 1989, *MNRAS*, 237, 1067
- Lutz, D., Genzel, R., Kunze, D., Spoon, H. W. W., Sturm, E., Sternberg, A., & Moorwood, A. F. M. 1998, *ASP Conf. Ser.* 132: *Star Formation with the Infrared Space Observatory*, 132, 89
- Lutz, D., Maiolino, R., Spoon, H. W. W., & Moorwood, A. F. M. 2004, *A&A*, 418, 465
- Maiolino, R., & Rieke, G. H. 1995, *ApJ*, 454, 95
- Maiolino, R., Ruiz, M., Rieke, G. H., Keller, L. D. 1995, *ApJ*, 446, 561
- Mason, R. E., Geballe, T. R., Packham, C., Levenson, N. A., Elitzur, M., Fisher, R. S., Perlman, E. 2006, *ApJ*, 640, 2 (astro-ph/0512202)
- Mauch, T., Murphy, T., Buttery, H. J., Curran, J., Hunstead, R. W., Piestrzynski, B., Robertson, J. G., & Sadler, E. M. 2003, *MNRAS*, 342, 1117
- McAlary, C. W., & Rieke, G. H. 1988, *ApJ*, 333, 1
- Merritt, D., & Ferrarese, L. 2001, *ApJ*, 547, 140
- Nenkova, M., & Ivezić, Ž., & Elitzur, M. 2002, *ApJ*, 570, L9
- Neugebauer, G., & Matthews, K. 1999, *AJ*, 118, 35
- Norman, C., & Scoville, N. 1988, *ApJ*, 332, 124
- Osterbrock, D. E. 1993, *ApJ*, 404, 551
- Panagia, N., & Felli, M. 1975, *A&A*, 39, 1
- Perez Garcia, A. M., Rodriguez Espinosa, J. M. 2001, *ApJ*, 557, 39
- Phillips, M. M. 1979, *ApJ*, 227, L121
- Pier, E. A., & Krolik, J. H. 1992, *ApJ*, 401, 99
- Pier, E. A., & Krolik, J. H. 1993, *ApJ*, 418, 673
- Polletta, M., Courvoisier, T. J.-L., Hooper, E. J., & Wilkes, B. J. 2000, *A&A*, 362, 75
- Rees, M. J. 1984, *ARA&A*, 22, 471
- Rieke, G. H. 1978, *ApJ*, 226, 550
- Risaliti, G., Elvis, M., Fabbiano, G., Baldi, A., & Zezas, A. 2005, *ApJ*, 623, L93
- Rodriguez Espinosa, J. M., Perez Garcia, A. M., Lemke, D., Meisenheimer, K. 1996, *A&A*, 315, L129
- Röttgering, H., Jaffe, W., Meisenheimer, K., Sol, H., Leinert, C., Richichi, A., Wittkowski, M. 2005, *Proc.SPIE*, 5491, "New Frontiers in Stellar Interferometry" (astro-ph/0507236)
- Rowan-Robinson, M., & Crawford, J. 1989, *MNRAS*, 238, 523
- Rush, B., Malkan, M. A., & Spinoglio, L. 1993, *ApJS*, 89, 1
- Sanders, D. B., Soifer, B. T., Elias, J. H., Madore, B. F., Matthews, K., Neugebauer, G., & Scoville, N. Z. 1988, *ApJ*, 325, 74
- Shang, Z., & Wills, B. 2004, *ASP Conf. Ser.* 311: *AGN Physics with the Sloan Digital Sky Survey*, 311, 13
- Shields, G. A. 1999, *PASP*, 111, 661
- Siebenmorgen, R., Haas, M., Krügel, E., Schulz, B. 2005, astro-ph/0504263
- Siebenmorgen, R., Krügel, E., & Spoon, H. W. W. 2004, *A&A*, 414, 123
- Spinoglio, L., & Malkan, M. A. 1989, *ApJ*, 342, 83
- Storchi-Bergmann, T., González Delgado, R. M., Schmitt, H. R., Cid Fernandes, R., & Heckman, T. 2001, *ApJ*, 559, 147
- Thean, A., Pedlar, A., Kukula, M. J., Baum, S. A., & O’Dea, C. P. 2000, *MNRAS*, 314, 573

- Thean, A., Pedlar, A., Kukula, M. J., Baum, S. A., & O’Dea, C. P. 2001, *MNRAS*, 325, 737
- Tran, H. D. 2003, *ApJ*, 583, 632
- Urry, C. M., & Padovani, P. 1995, *PASP*, 107, 803
- Veilleux, S., Kim, D.-C., Sanders, D. B., Mazzarella, J. M., & Soifer, B. T. 1995, *ApJS*, 98, 171
- Ulvestad, J. S., Wrobel, J. M., Roy, A. L., Wilson, A. S., Falcke, H., & Krichbaum, T. P. 1999, *ApJ*, 517, L81
- Véron-Cetty, M.-P., & Véron, P. 2003, *A&A*, 412, 399
- Ward, M., Elvis, M., Fabbiano, G., Carleton, N. P., Willner, S. P., & Lawrence, A. 1987, *ApJ*, 315, 74
- Weedman, D. W., Hao, L., Higdon, S. J. U., Devost, D., Wu, Y., Charmandaris, V., Brandl, B., Bass, E., Houck, J. R. 2005, *astro-ph/0507423*
- White, R. L., Becker, R. H., Helfand, D. J., & Gregg, M. D. 1997, *ApJ*, 475, 479
- Xu, C., Livio, M., & Baum, S. 1999, *AJ*, 118, 1169